Throw-rate variations within linkage zones during the growth of normal faults: case studies from the Western Volcanic Zone, Iceland.

Francesco Iezzi[1*], Gerald Roberts[1], Joanna Faure Walker[2]

[1]Department of Earth and Planetary Sciences, Birkbeck, University of London, Malet Street, London, WC1E 7HX, UK

[2] Institute for Risk and Disaster Reduction, University College London, Gower Street, London, WC1E 6BT, UK

*Corresponding author: Francesco Iezzi, francesco.iezzi.15@ucl.ac.uk, +447928037318, Department of Earth and Planetary Sciences, Birkbeck, University of London, Malet Street, London, WC1E 7HX, UK

Abstract

This work investigates how throw-rates vary within fault bends and sites of fault linkage during the process of normal fault growth. In the Western Volcanic Zone, Iceland, through detailed field mapping and field measurements of fault throws, normal faults are mapped and along-strike throw profiles are constructed in order to understand how the throw-rates relate with the local fault geometry along faults at different stages of linkage. The results show that throw-rates increase within linkage zones and propagating fault bends independently from the stage of maturity of the fault bend. This implies that 1) the relationship between the local fault geometry and the along-strike distribution of throw-rate is driven by the deeper part of the fault, where established fault bends start propagating to the surface; 2) faults grow first by

linkage and coalescence of separate faults, and then by accumulation of slip on the resultant fault, in agreement with models of fault growth by linkage and coalescence; 3) incipient fault bends can produce uncertainty associated with palaeoseismological results, if fault bends remain unrecognised. Moreover, this work demonstrates that existing models showing increased co-seismic and throw-rates within fault bends and sites of fault linkage found in continental extensional settings are valid in a geodynamic context of a mid-oceanic rifts.

Introduction

The growth of along-strike fault bends on normal faults can be described as a consequence of the linkage of either originally isolated fault segments during fault growth processes (isolated fault model) or individual fault segments that grow as kinematically related components of a fault array (coherent fault model) (e.g. MacLeod et al., 2000; Manfield and Cartwright, 2001; Manfield and Kattenhorn, 2001; Jackson et al., 2002; Walsh et al., 2003; Gawthorpe et al., 2003; Tentler and Mazzoli, 2005; Villemin and Bergerat, 2013; Rotevatn et al., 2018). Fault growth models show that once en echelon fault segments are linked, and a fault bend is established to link the faults, the throw-rates along the newly formed fault increase to re-establish the displacement-length scaling following the length increase (e.g. Cowie and Roberts, 2001). Moreover, field measurements have highlighted the occurrence of throw and throw-rate enhancements within along-strike fault bends that form at sites of fault linkage in response to local anomalies in strike and dip within the bend, especially where the fault dip value is relatively high and the horizontal strain-rate is maintained (Figure 1a; Faure Walker et al., 2009; Wilkinson et al., 2015; Mildon et al., 2016; Iezzi et al., 2018; Iezzi et al., 2019). These findings are supported by theoretical studies showing that the vertical offset (throw) on

a normal fault is controlled by the local fault geometry and the extension that the fault must accommodate at that location (Figure 1b; Faure Walker et al., 2009; 2010). However, there is a lack of studies describing in detail whether this relationship applies also during the fault growth and the propagation of the fault bends. Therefore, to expand our knowledge on how faulting develops within along-strike fault bends, we need to study how the throw and the throw rate within fault bends evolve during the propagation and establishment of fault bends throughout the process of fault growth.

The Western Volcanic Zone (WVZ) in Iceland (Figure 2) has been widely studied in order to understand the mechanisms of fault growth because it is characterised by the continuous propagation of active faults upwards through subsequent lava flows (Gudmundsson, 1987; 1992; 2000; Saemundsson, 1992; Acocella et al., 2000; Bull et al., 2003; Grant and Kattenhorn, 2004; Sinton et al., 2005; Friese, 2008; Sonnette et al., 2010; Villemin and Bergerat, 2013; Trippanera et al., 2015; Weismuller et al., 2019). Different models of fault bend growth in this region have been proposed, explaining the development of bends as fault segments growing to connect two principal en-echelon faults (e.g. Acocella et al., 2000), and as a response to local perturbations of the stress field in the region of the bend (Grant and Kattenhorn, 2004). However, these previously published models did not use time constraints in order to understand the evolution of the throw-rate within the fault bend during its onset and development. Furthermore, although normal faults within the WVZ have been widely studied (e.g. Gudmundsson, 1987; Friese; 2008; Sonnette et al., 2010), none of them have analysed the relationship between the local fault geometry and the distribution of throw and throw-rates along the strike of the fault.

In this paper we study faults in the Thingvellir rift and the Hengill volcanic complex, located in the Western Volcanic Zone (WVZ) in Iceland, through detailed field mapping and measurements of the throw along the strike of the faults. Due to ongoing propagation through young lavas, these faults preserve a variety of different stages of fault linkage maturity (Figure 1c). These faults allow us to examine a spectrum of cases from where the principal fault segments are not physically connected (soft-linkage) to cases where the principal fault segments are connected with well-established fault bends (hard-linkage). We describe what observations of these different geometries suggest for the evolution of throw and throw-rates during the development of along-strike fault bends. We discuss the implications of these findings for the processes of fault growth and for the interpretation of palaeoseismological studies. Furthermore, at the time of writing the relationships between the local non-planar fault geometry and the along-strike distribution of throw has been observed only within zones of continental extension (Faure Walker et al., 2009; 2015; Iezzi et al., 2018). The study of faults in Iceland's WVZ allows us to test if the local non-planar fault geometry exerts a control on the along-strike distribution of throw also in a geodynamic context of a plate boundary such as the Mid Atlantic Ridge.

Geological background

Iceland is located on a plateau generated by the intersection between the Mid-Atlantic Ridge and a mantle plume, which caused locally thick oceanic crust, a broad topographic high and the emergence of the oceanic ridge (Figure 2a; Wolfe et al., 1997). In Iceland, the Mid-Atlantic Ridge is characterized by two main rift segments: the first is located on the western side of the island, composed by the Reykanes Ridge (RR) and the Western Volcanic zones (WNZ); the second is located on the eastern side of the island, composed by the Eastern

Volcanic Zone (EVZ) and the Northern Volcanic Zone (NVZ) (Figure 2a). These two main segments are connected by the South Iceland Seismic Zone (SISZ) and the Central Iceland Volcanic Zone (CIVZ) (Figure 2a). Those volcanic zones, which represent the centre of spreading across the plate boundary, consist of a complex system formed by central volcanoes, fissure swarms 5-20 km wide and 10s to >100 km long, and fault rift systems that strike approximately normal to the spreading direction (Einarsson, 2008). Transform zones, such as the SISZ, are areas where the plate boundary runs parallel to the spreading direction and the deformation is accommodated by distributed faulting, rather than being confined to a single transform fault (Bergerat and Angelier, 2000; Einarsson 2008).

GPS observations show that the overall spreading rate across Iceland is about 18-20 mm/yr and it is not equally distributed across the different Mid Atlantic Ridge segments (Figure 2a; LaFemina et al., 2005; Perlt and Heinert, 2006; Geirsson et al., 2010). Spreading rates across the WVZ vary between 3-8 mm/yr, with an overall decrease towards the NE (LaFemina et al., 2005; Perlt and Heinert, 2006; Geirsson et al., 2010). Spreading rates across the EVZ vary between 11-19 mm/yr, with an overall increase towards the NE (LaFemina et al., 2005).

The Thingvellir rift and the Hengill volcanic complex, which are both part of the WVZ, occur north and south of the Thingvallatavn lake, a large catchment produced by extensive subsidence within the rift zone (Figure 2b; Saemundsson, 1992; Bull et al., 2003). The Thingvellir rift is a narrow rift system trending about N30º, expressed at the surface by a series of normal faults and extension fractures striking mostly sub-parallel to the trend of the WVZ on both sides of the rift (Figure 2c; Gudmundsson, 1987; Grant and Kattenhorn, 2004; Friese, 2008; Sonnette et al., 2010). At Thingvellir, faults propagate through post-glacial Holocenic lava flows which have filled the rift valley in the last ~10 kyr (Figures 2c;

Saemundsson, 1992; Sinton et al., 2005). The Hengill Volcanic complex is characterized by a central volcano and a dense set of normal faults striking about N30º and dissecting Pleistocene basaltic lava flows and hyaloclastites deposits, with extensive activity also during the Holocene (Figure 2d; Gudmundsson, 1995; Friese, 2008).

Methods

We carried detailed field mapping in order to produce structural fault maps and densely-spaced (measurements collected every ~50 m) along-strike throw and throw-rate profiles for (1) the Almannagja fault, together with a study of the evolution of the footwall drainage following fault linkage; (2) for four W-dipping faults distributed within and on the eastern flank of the Thingvellir rift; (3) for three normal faults within the Hengill volcanic complex, where we produced also a map of the offsets of a glacial erosion surface preserved during the demise of the glaciation (Figure 2).

Structural fault maps in Thingvellir and Hengill have been produced combining published maps (Gudmundsson, 1987; Saemundsson, 1992; Sinton et al., 2005; Sonnette et al., 2010), Google Earth imagery and our own fieldwork. Fault scarp profiles were constructed using a *Trupulse 360R*® laser range finder, which allows us to measure the azimuth, the vertical distance and the horizontal distance between the observer and the point of interest with an accuracy of ±30 cm per single measurement. Fault scarp profiles were constructed by hitting a dense distribution of clear reflectors with the laser (e.g. outcropping surfaces of basaltic lava flows) distributed along the same azimuth, recording the relative vertical and horizontal distances of each measurement from the observer. The vertical and horizontal distances have been plotted in order to reconstruct a fault scarp profile that allows the fault throw to be

149 measured (Figures 3a and 3b). The scarp profiles are built normal to the fault strike, so to
150 avoid effects of apparent dip.
151
152 In Thingvellir, most faults and extension fractures exhibit a dilatational component between
153 the footwall and hangingwall (Figure 3), so measurements of the vertical component of slip
154 have been used to differentiate between faults and extensional fractures. Faults are defined as
155 fractures with more than 1 m of vertical slip; extension fractures are defined as fractures with
156 a vertical slip less than 1 m. For the Almannagja fault, which shows a prominent monocline
157 in the hangingwall, we constructed serial fault scarp profiles with an along-strike spacing of
158 about 50 m (Figure 3a and b). Where it was not possible to take measurements across the
159 monocline, measurements of the distance between the observer and (1) the inflection point at
160 the base of the monocline (i.e. the point where the hangingwall starts to bend towards the
161 footwall), (2) the top of the monocline and (3) the top of the footwall were collected (Figures
162 3a and b). The throw is defined as the vertical distance between the inflection point at the
163 base of the monocline and the top of the footwall (Figures 3a and b). Offsets across the
164 southern part of the fault could not be measured because the inflection of the monocline is
165 below the lake level (Figures 4e and 5). For the W-dipping faults 1 and 2 (thereafter referred
166 as WDf1 and WDf2), the throw was defined as the vertical offset between the top of the
167 hangingwall and top of the footwall (Figures 3c). For the W-dipping fault 3 (thereafter
168 referred as WDf3), which is part of the Hrafnagja fault (*sensu* Gudmunsson, 1987), due to
169 dense vegetation and the difficulty of constructing across-fault profiles, the throws have been
170 derived by building along-strike topographic profiles of the tops of the hangingwall and of
171 the footwall from one observation point and then measuring the relative vertical distance
172 between the two profiles (Figures 3c). The W-dipping fault 4 (thereafter referred as WDf4),
173 which is part of the Gildruholtsgja fault (*sensu* Gudmundsson, 1987), does not show a

dilatational component between footwall and hangingwall, and the throw is measured with across-strike fault scarp profiles as the vertical offset of the footwall and the hangingwall surfaces across the fault scarp (Figures 3d). For the Thingvellir rift, throw-rates are calculated using time constraints from ages of the lava flows displaced by the faults (Figures 2b, 5 and 10; from Sinton et al., 2005). The age constraints of the lava flows, dated between ~10200 and ~8200 years BP, are derived combining ^{14}C-dating, tephrocronology and chemical analyses from major and trace elements (Figures 4 and 5; Sinton et al., 2005).

For Hengill, a set of W-dipping normal faults has been mapped in detail, together with a dissected subglacial erosional surface, produced by the erosive action of the glacier on the landforms beneath it. Serial fault scarp profiles have been constructed across the normal faults, and the throw in each profile has been constrained measuring the offset between subglacial erosional surfaces in the hangingwall and footwall (Figures 3d). For Hengill, the cosmogenic exposure ages of these erosional surfaces were used as a constraint to calculate the throw rate of the faults (Licciardi et al., 2007). We do this because we assume that the erosive process of a moving glacier would not have allowed preservation of fault scarps, and therefore these started to be preserved only once the deglaciation occurred, causing the exposure of the eroded surfaces. Measurements of the cosmogenic ^{3}He concentrations in olivine phenocrysts, collected from different erupted basaltic lava caps of table mountains located within the WVZ, show that the exposure age of these lava flows occurred when the ice melted during the deglaciation between 7.2 ka and 13 ka (from Licciardi et al., 2007). Hence, we can infer an exposure age of the subglacial erosional surfaces in Hengill comprised between 7.2 ka and 13 ka. This time range is used to constrain the fault throw-rates for Hengill.

We built along-strike throw and throw rate profiles for each fault projecting the throw measurements along the principal strike of the fault, obtained using strike lines (Figures 7, 11 and 14). The along-strike profiles are compared with the fault traces to examine whether the local fault geometry affects the distribution of throw and throw-rates along the fault.

Results

Thingvellir rift

Almannagja Fault

The Almannagja fault is a complex fault system about 7.1 km long with a dip towards the SE and strike of N033º. It comprises linked fault segments, up to 1 km long, arranged with end-on and en-echelon distributions (Figures 4, 5 and 6). The Almannagja fault is characterized by a vertical footwall scarp and a broad monocline which connects the footwall with the rift valley (Figures 3a, 3b, 4a, 4b, 4c, 4e, 5 and 6). An inner graben-like structure developed between the footwall and the monocline with minor antithetic faults that delimit the SE flank of the graben (Figures 3a, 3b, 4a, 4d, 4e, 5 and 6). In some places along the fault, the monocline is dissected by multiple antithetic faults (Figures 3a, 4a, 4d, 5 and 6). The fault segments distributed with en-echelon arrangements are, in most cases, linked by extension fractures propagating through the footwall of the fault (Figures 3b, 4a, 4d, 5 and 6). We interpret these fractures as the palaeoterminations of the principal fault segments prior to fault linkage (palaeo-tips, *sensu* McLeod et al. 2002). Our observations suggest that the shape of the monocline reflects the segmentation of the Almannagja fault. Where the fault segments of the Almannagja fault are longer and more continuous, the inflection line of the monocline is continuous and consistent along the strike of the fault (Figures 5, 6 and 7). Where the single faults are shorter and less continuous, the inflection line becomes less regular and moves closer to the fault trace (Figures 5, 6 and 7). The tips of the Almannagja fault are

characterized by the base monocline inflection line approaching or joining the fault, a decrease of the height of the vertical fault scarp and of the monocline and by a predominance of extension fractures (Figures 4f, 5 and 6).

The along-strike throw profile of the Almannagja fault has a multi-humped shape, with an overall increase of throw towards the south (Figure 7). The maximum measured throw is about 39 m, located in what appears to be the central part of the entire Almannagja fault. The comparison between the multi-humped throw profile and the fault geometry allows us to identify three principal fault segments of the overall Almannagja fault (Figure 7). A well-defined along-strike fault bend links two of the main segments of the Almannagja fault, herein called Segment 1 and Segment 2, accommodating an overall right step of the fault trace in a position where a palaeo-tip indicated the presence of a former relay zone (Figure 6b, 7). Within the fault bend the throw anomalously increases, causing the throw profile of the Segment 2 to have a double peak of about 31 m. Segment 2 and Segment 3 are soft-linked in a left en-echelon arrangement (Figure 7). Because of the vegetation, it was not possible to obtain measurements across the southern part of Segment 3, and therefore it is not clear how the throw changes along the fault in that location. Other smaller bends exist along the fault, connecting single small fault segments, but the resolution of the throw measurements (every 50 m along strike) does not allow us to study variations of throw across bends shorter than this distance. The width of the monocline confirms the principal segmentation of the Almannagja fault. The monocline tips out in the relay zone between Segment 2 and Segment 3, in agreement with the soft-linkage between the two fault segments (Figures 5, 6 and 7). Note that the monocline does not tip out at the fault bend linking Segment 1 and Segment 2, but does narrow, reflecting the hard-linkage between the two fault segments (Figures 5, 6 and 7).

In summary, the Almannagja fault consists of several individual fault segments linked by faults propagating within linkage zones and forming along strike fault bends. The comparison between the fault geometry and the multi-humped throw profile allows us to subdivide the fault into three principal fault segments. A prominent along-strike fault bend links two of these principal fault segments, within which the throw and the throw-rates anomalously increase if compared with the values of throw and throw rate outside the fault bend.

Influence of the fault linkage on the drainage system.

The drainage system in the footwall of the Almannagja fault is studied to observe how the fault evolution has influenced the river flow through time (Figure 8). This provides important insights to understand the timings of the fault linkage and of the propagation of fault bends at the surface. The footwall of the fault is marked by the presence of a river flowing south-eastwards and towards the rift valley (Figure 8a and 8b). The river crosses the Almannagja fault at a spectacular waterfall (Figures 8c and 8d), in the position of a former en echelon step between two faults, now marked by a fault bend and preserved palaeo-tip (Fig. 8b and c). Both the river bed and the waterfall are located to the north of the maximum peak in throw of the Almannagja fault (see location of the waterfall in the throw profile in Fig. 7). As shown in Fig. 8b, an abandoned river bed is located to the southwest of the present river. We combine these observations to suggest that the fault linkage can be one of the plausible geologic processes that has influenced the drainage in the footwall of the Almannagja fault, causing a northward migration of the river bed. The fault linkage causes an increase of the throw-rates along the entire fault, with faster throw-rates located within the central part of the fault (e.g. Cowie and Roberts, 2001). The initial river course flowed through the en echelon step, with

recent linkage forming a bend occurring rapidly so that the waterfall formed, and has not had time to produce an incised slot gorge due to headward erosion (*sensu* Whittaker et al., 2007). We suggest that a rapid increase of the throw-rates during linkage allowed footwall uplift to outpace headward erosion and incision by the river, with off-fault footwall uplift diverting the course of the river to NE away from the growing uplift at the fault centre, SW of the river.

W-dipping faults

Several W-dipping faults are accommodating the regional extension across the Thingvellir rift. We focused our attention on two faults located in the immediate hangingwall of the Almannagja fault (WDf1 and WDf2), and on two faults bounding the eastern flank of the rift valley (WDf3 and WDf4; Figures 2c, 9 and 10).

The WDf1 and WDf2 are both formed by mostly subparallel small fault segments with a dilatational component, organized in en-echelon and end-on arrangements, dissecting lava flows dated to ~9000 years BP (Figures 9a, 9b, 9c, 9d and 10a; Sinton et al., 2005). Extensional fractures accommodate the deformation within the relay zones of the en-echelon distributed segments boundaries (Figures 9a, 10a, 11a and 11b). Both the along-strike throw profiles present multiple maxima, reflecting an immature stage of the fault growth (Figures 11a and 11b). However, both faults present relative maxima in throw and throw-rates on the fault segments immediately outside the linkage zones, across relay zones and incipient fault bends linking fault segments (Figures 11a and 11b). Hence, our results suggest that the fault throw increases within newly formed linkage zones along immature faults (Figure 11a and 11b). Again, other relative maxima might exist across smaller relay zones and incipient

298 bends, but it is not possible to study these because of the resolution of the field
299 measurements.
300
301 The fault traces of WDf3 and WDf4 are more continuous than WDf1 and WDf2, and both
302 present along-strike fault bends in their traces (Figures 9e, 9f, 9g, 9h, 10b). The WDf3 is
303 formed by fault segments with a dilatational component, and it is also marked by two small
304 antithetic faults accommodating the deformation in the hangingwall (Figures 10b and 11c). In
305 the southern part of the fault trace the fault is propagating through a relay zone connecting
306 two en-echelon fault segments, forming an incipient fault bend (Figures 9f, 10b and 11c).
307 The throw profile shows an increase of the throw within the fault bend compared with the
308 values of throw immediately outside the bend (Figure 11c). The WDf4 has a more continuous
309 fault trace, characterized by a classic fault scarp without an obvious dilatational component
310 (Figures 9g, 9h, 10b and 11d). The fault trace presents a mature along-strike fault bend,
311 within which the throw and throw-rates profiles have relative maxima, when compared to
312 values of throw and throw-rates immediately outside the bend (Figure 10b and 11d).
313
314 In summary, normal W-dipping faults distributed within the Thingvellir rift are characterized
315 by different stages of the process of fault growth and linkage, which is reflected in different
316 stages of maturity of relay zones and fault bends. Independently to the stage of maturity of
317 the fault bend, all the studied faults present increased throw and throw-rates within fault
318 bends.
319
320 ***Hengill volcanic complex***
321

Faults in the Hengill volcanic complex are prominently fault scarps, often with slope deposits at the base of the scarp, propagating through hyaloclastites and basaltic lava flows (Figures 3d, 12a, 12b, 12d, 12e and 13). In two locations, outcrops of striated fault planes show dip-slip kinematics (Figures 12d and 13). Subglacial flat erosional surfaces, the products of the erosional activity of the moving glacier on the volcanic deposits, are located on both the hangingwall and the footwall of the faults (Figures 12a, 12b, 12c, 12e and 13). The glacial origin of these surfaces is confirmed by the presence of erratic boulders on top of them (Figure 12c).

The analysis of our field data allows us to identify three principal fault segments (Figure 14). Fault 1 has a skewed along-strike throw profile, with maxima in throw values located within a fault bend in the strike of the fault (Figure 14). Fault 2 has a fault bend towards its northern mapped extent, across which the throw profile of Fault 2 achieves a relative maximum (Figure 14). Overall, these two fault bends define a broad fault bend for the mapped set of faults (Figure 14). The cumulative throw and throw rate profiles present two maxima, with one of them located within the broad fault bend (Figure 14). Moreover, it is interesting to note that a lake is located in the hangingwall of the broad fault bend, coincident with the maximum measured throw and between the two fault bend segments identified on Fault 1 and Fault 2 (Figure 14). This prompts the idea that the maximum throw within the fault bend might have affected the drainage system in the hangingwall of the fault, causing a maximum hangingwall subsidence in front of the bend. Hence, these results suggest that the local fault geometry can affect the spatial distribution of throw and throw-rates along normal faults in this example.

Discussion

This study of faults in the Thingvellir and Hengill regions suggests that faults within the Western Volcanic Zone in Iceland are characterized by different stages of fault growth, and this is reflected in different stages of maturity of the linkage zones and of the along-strike fault bends. The comparison between the local fault geometry and the spatial distribution of throw and throw-rates shows that, independently to the stage of maturity of the fault bends, the throw and throw-rates anomalously increase within the bends.

These findings can improve our knowledge on the progressive development of faulting within fault bends, because previous works studying throw and throw-rate enhancement within fault bends have been focussed on well-established fault bends at the surface (Faure Walker et al., 2009, 2015; Wilkinson et al., 2015; Mildon et al., 2016; Iezzi et al., 2018; 2019). Here, for the first time, it is shown that throw-rate enhancements also occur in incipient fault bends, where the propagation of fault and the formation of the fault bend is not complete. In cases where the principal fault segments are soft-linked, with immature fault bends growing in the linkage zone, the throw values of the two principal single faults increase towards the linkage zone, suggesting that the throw will eventually be larger within the fault bend once it is fully formed at the surface. These findings could be corroborated using high quality digital elevation models (DEM) (e.g. Weismuller et al., 2019), which at the time of writing have not been used to study the relationships between linkage zones and throw values.

Overall, our results suggest that the relationship between the non-planar fault geometry and the conservation of the strain-rate along the fault, which causes throw-rate enhancements in response to changes in strike and dip within fault bends with constant horizontal extension

372 (Faure Walker et al., 2009, 2015), might be driven from processes occurring on the fault at
373 depth, where fault bends enucleate, establish their geometry and propagate towards the
374 surface (e.g. see Iezzi et al. 2018, their Figure 2).
375
376 These findings can also help to improve the knowledge of the process of fault growth by
377 linkage of previously individual fault segments (Figure 15). If the variation of strike and dip,
378 with dip that has been shown to increase within bends for a variety of normal faults (Iezzi et
379 al., 2018), promotes high throw-rates in incipient bends due to conservation of heave (Fig.
380 15a; Faure Walker et al., 2009), local throw and displacement maxima may develop (Fig.
381 15b). The upward propagation of established faults at depth causes the development of new
382 fault segments at the surface. As the newly formed individual faults grow in length, they start
383 to link. In response to the fault linkage, the throw-rates along the entire fault work to create
384 an along-strike profile consistent with a single longer fault, but local maxima in throw-rates
385 will be located within the fault bends. However, note that development of such maxima
386 depend on the relative values of strike and dip in the fault bend and along intervening
387 segments, and also, presumably, the magnitude of rotations about horizontal axes in relay
388 zones (e.g. see Walsh et al. 2003; their Fig. 4); note that we were unable to resolve such
389 rotations due to the short time window recorded by the deformation we measure (<10-12 ka)
390 and the resultant low magnitude of the rotations. Our suggestion is consistent with classic
391 models of fault growth by linkage, where the fault length is established early followed by
392 accumulation of the finite fault slip, and it can apply for either cases of faults previously
393 isolated or for cases where surface faults are kinematically related components of a fault
394 array (Walsh et al., 2002; 2003; Nicol et al., 2005). The key point we want to emphasise is
395 that local maxima may develop in fault bends. Throw enhancements within incipient fault
396 bends could be one possible explanation of the wide scatter in natural values of displacement

accrual occurred during fault lengthening (10-60% of faults displacement cumulated during faults lengthening; Rotevatn et al., 2018). If the measurements of maximum displacement, obtained at different stages of fault lengthening and used within displacement versus fault length diagrams, were collected across fault bends, this might create a scatter of the values of maximum displacement used to study the fault evolution through time.

The increases of throw-rate within incipient fault bends have implications for palaeoseismology. Previous studies show that fault bends may be the site of anomalously high coseismic throws (e.g. Iezzi et al., 2018). If fault bends are not recognised, this could lead to overestimates of palaeoearthquake magnitudes from palaeoseismological trenches (Sgambato et al., 2020).

Overall, this study suggests that the throw and throw-rate distributions along faults within the WVZ are influenced by the local fault geometry and the strain that the fault must accommodate in that location, following the model first presented in Faure Walker et al. (2009). This implies that the relationship between the non-planar fault geometry and the conservation of strain along the fault and across fault bends, which causes throw rate enhancements within the bends, is valid also in an extremely fast-deforming geodynamic domain such as the Mid-Atlantic Ridge. Therefore, this work highlights the importance of including the effects of non-planar fault geometry on the seismic behaviour of normal faults also in seismic hazard assessments located in geodynamic contexts different from the Central Apennines, where the first examples have been identified (Faure Walker et al., 2018).

Conclusions

Detailed fault mapping and serial fault scarp profiles were carried out along 5 normal faults in the Thingvellir rift and 3 normal faults in the Hengill Volcanic Complex, both located in the WVZ, Iceland. Normal faults within the WVZ in Iceland present different stages of fault growth, which is reflected in a variety of stages of maturity of along-strike fault bends connecting the principal fault segments. Along-strike throw and throw rate profiles show that, independently to the stage of maturity of the fault bends, the throw and throw-rates increase within the fault bends, compared to the values on the fault segments immediately outside the bends. This implies that: 1) the relationship between the local fault geometry and the conservation of the strain rate, which causes throw and throw rate enhancements within the bend in response to local changes in strike and dip within the bend with constant horizontal strain, might be driven by processes occurring in the deeper part of the fault; 2) during fault growth, fault bends in linkage zones are propagating faster than the slip accumulation of the principal fault segments, implying that during the process of fault growth by linkage and coalescence the fault works in order to first establish the fault length and then to accumulate slip; 3) palaeoseimological studies must take in account the effect of incipient fault bends on the throw-rates of a fault, in order to avoid misleading interpretations of results obtained from palaeoseimological trenches located in proximity of incipient bends. Overall, this work shows that the previously observed relationship between the non-planar fault geometry and the conservation of strain rate along a fault affects the seismic behaviour of a normal fault also in a geodynamic domain of a mid-oceanic ridge, implying that this relationship is valid also in geodynamic contexts different from the Central Apennines, where the first examples of this relationship have been identified.

Acknowledgments

446 This study was funded by NERC Studentship NE/L002485/1 to Iezzi. We thank Steve Hirons
447 for the help during the fieldwork. The research data used in this work are all exhibited in the
448 paper.
449
450 **References**
451
452 Acocella, V., A. Gudmundsson, and R. Funiciello (2000), Interaction and linkage of
453 extension fractures and normal faults: examples from the rift zone of Iceland, Journal of
454 Structural Geology, 22(9), 1233-1246. https://doi.org/10.1016/S0191-8141(00)00031-6
455 Bergerat, F., and Angelier, J. (2000), The South Iceland Seismic Zone: tectonic and
456 sismotectonic analyses revealing the evolution from rifting to transform motion,
457 Journal of Geodynamics, 29(3-5), 211-231. https://doi.org/10.1016/S0264-
458 3707(99)00046-0
459 Bull, J. M., T. A. Minshull, N. C. Mitchell, K. Thors, J. K. Dix, and A. I. Best (2003), Fault
460 and magmatic interaction within Iceland's western rift over the last 9 kyr, Geophysical
461 Journal International 154, no. 1 (2003): F1-F8 https://doi.org/10.1046/j.1365-
462 246X.2003.01990.x
463 Cowie, P.A. and G.P. Roberts (2001), Constraining slip rates and spacings for active normal
464 faults. Journal of Structural Geology, 23(12), pp.1901-1915
465 https://doi.org/10.1016/S0191-8141(01)00036-0
466 Einarsson, P. (2008), Plate boundaries, rifts and transforms in Iceland, Jökull, 58(12), 35-58.
467 Faure Walker, J. P., F. Visini, G. Roberts, C. Galasso, K. McCaffrey and Z. Mildon (2018),
468 Variable fault geometry suggests detailed fault□slip□rate profiles and geometries are
469 needed for fault□based probabilistic seismic hazard assessment (PSHA), Bulletin of
470 the Seismological Society of America, 109(1), 110-123.

471 Faure Walker J.P., G. P. Roberts, P. A. Cowie, K. McCaffrey. L. Wedmore, Z. Watson, L. C.
472 Gregory (2015), Long-term strain rates as a tool for understanding the mechanics of
473 continental extension and the importance of local 3D fault geometry for local throw-
474 rates across faults. 6th Int. INQUA Meeting on Paleoseismology, Active Tectonics and
475 Archaeoseismology, 19-24 April 2015, Pescina, Fucino Basin, Italy, 27 150-154.
476 Faure Walker, J. P., G. P. Roberts, P. R. Sammonds, and P. A. Cowie (2010), Comparison of
477 earthquake strains over 10 2 and 10 4 year timescales: Insights into variability in the
478 seismic cycle in the central Apennines, Italy, *J. Geophys. Res.*, *115*(B10), B10418,
479 doi:10.1029/2009JB006462.
480 Faure Walker, J. P., G. P. Roberts, P. A. Cowie, I. D. Papanikolaou, P. R. Sammonds, A. M.
481 Michetti, and R. J. Phillips (2009), Horizontal strain-rates and throw-rates across
482 breached relay zones, central Italy: Implications for the preservation of throw deficits at
483 points of normal fault linkage, *J. Struct. Geol.*, *31*(10), 1145–1160,
484 doi:10.1016/j.jsg.2009.06.011.
485 Friese, N (2008), Brittle tectonics of the Thingvellir and Hengill volcanic systems, Southwest
486 Iceland: field studies and numerical modeling, Geodinamica Acta, 21:4, 169-185, DOI:
487 10.3166/ga.21.169-185
488 Gawthorpe, R. L., C. A. L. Jackson, M. J. Young, I. R. Sharp, A. R. Moustafa and C. W.
489 Leppard (2003), Normal fault growth, displacement localisation and the evolution of
490 normal fault populations: the Hammam Faraun fault block, Suez rift, Egypt. Journal of
491 Structural Geology, 25(6), 883-895. https://doi.org/10.1016/S0191-8141(02)00088-3
492 Geirsson, H., T. Árnadóttir, S. Hreinsdóttir, J. Decriem, P. LaFemina, S. Jónsson,... and T.
493 Villemin (2010), Overview of results from continuous GPS observations in Iceland
494 from 1995 to 2010. Jökull, 60, 3-22.
495 Grant, J. V., & Kattenhorn, S. A. (2004), Evolution of vertical faults at an extensional plate

boundary, southwest Iceland, Journal of Structural Geology, 26(3), 537-557. https://doi.org/10.1016/j.jsg.2003.07.003

Gudmundsson, A. (2000), Fracture dimensions, displacements and fluid transport. Journal of Structural Geology, 22(9), 1221-1231. https://doi.org/10.1016/S0191-8141(00)00052-3

Gudmundsson, A. (1995), Infrastructure and Mechanics of Volcanic Systems in Iceland, Journal of Volcanology and Geothermal Research, vol. 64, no. 1-2, 1995, pp. 1–22., doi:10.1016/0377-0273(95)92782-q.

Gudmundsson, A. (1992), Formation and growth of normal faults at the divergent plate boundary in Iceland, Terra Nova, 4,464-471, 1992. https://doi.org/10.1111/j.1365-3121.1992.tb00582.x

Gudmundsson, A. (1987), Geometry, formation and development of tectonic fractures on the Reykjanes Peninsula, southwest Iceland. Tectonophysics, 139(3-4), 295-308. https://doi.org/10.1016/0040-1951(87)90103-X

Iezzi, F., G. Roberts, J. F. Walker and I. Papanikolaou (2019), Occurrence of partial and total coseismic ruptures of segmented normal fault systems: Insights from the Central Apennines, Italy, Journal of Structural Geology, 126, 83-99. https://doi.org/10.1016/j.jsg.2019.05.003

Iezzi, F., Z. Mildon, J. F. Walker, G. Roberts, H. Goodall, M. Wilkinson, and J. Robertson (2018), Coseismic throw variation across along-strike bends on active normal faults: Implications for displacement versus length scaling of earthquake ruptures. Journal of Geophysical Research: Solid Earth, 123. https://doi.org/10.1029/2018JB016732

Jackson, C. A. L., R. L. Gawthorpe and I. R. Sharp (2002), Growth and linkage of the East Tanka fault zone, Suez rift: structural style and syn-rift stratigraphic response, Journal of the Geological Society, 159(2), 175-187. https://doi.org/10.1144/0016-764901-100

520 LaFemina, P. C., T. H. Dixon, R. Malservisi, T. Arnadottir, E. Sturkell, F. Sigmundsson, and
521 P. Einarsson (2005), Geodetic GPS measurements in south Iceland: Strain
522 accumulation and partitioning in a propagating ridge system, J. Geophys. Res., 110,
523 B11405, doi:10.1029/2005JB003675
524 Licciardi, J.M., Kurz, M.D. and Curtice, J.M., 2007. Glacial and volcanic history of Icelandic
525 table mountains from cosmogenic 3He exposure ages. Quaternary Science Reviews,
526 26(11-12), pp.1529-1546. https://doi.org/10.1016/j.quascirev.2007.02.016
527 McLeod, A. E., J. R. Underhill, S. J. Davies and N. H. Dawers (2002), The influence of fault
528 array evolution on synrift sedimentation patterns: Controls on deposition in the
529 Strathspey-Brent-Statfjord half graben, northern North Sea, AAPG bulletin, 86(6),
530 1061-1093. https://doi.org/10.1306/61EEDC24-173E-11D7-8645000102C1865D
531 McLeod, A. E., N. H. Dawers, J. R. Underhill (2000), The propagation and linkage of normal
532 faults: insights from the Strathspey-Brent-Statfjord fault array, northern North Sea.
533 Basin Research, 12, 263-284. https://doi.org/10.1046/j.1365-2117.2000.00124.x
534 Mansfield, C. and Cartwright, J. (2001), Fault growth by linkage: observations and
535 implications from analogue models. *Journal of Structural Geology*, 23, 745-763.
536 https://doi.org/10.1016/S0191-8141(00)00134-6
537 Mildon, Z. K., G. P. Roberts, J. P. Faure Walker, L. Wedmore, and K. J. W. McCaffrey
538 (2016), Active normal faulting during the 1997 seismic sequence in Colfiorito, Umbria:
539 Did slip propagate to the surface?, *J. Struct. Geol.*, doi:10.1016/j.jsg.2016.08.011.
540 Nicol, A., J. Walsh, K. Berryman, and S. Nodder (2005), Growth of a normal fault by the
541 accumulation of slip over millions of years. Journal of Structural Geology, 27(2), 327-
542 342. https://doi.org/10.1016/j.jsg.2004.09.002
543 Perlt, J., and Heinert, M. (2006), Kinematic model of the South Icelandic tectonic system,
544 Geophysical Journal International, 164(1), 168-175. https://doi.org/10.1111/j.1365-

246X.2005.02795.x

Podolsky, D. M., and Roberts, G. P. (2008), Growth of the volcano-flank Koa'e fault system, Hawaii, Journal of Structural Geology, 30(10), 1254-1263.

Rotevatn, A., C. A. L. Jackson, A. B. M. Tvedt, R. E. Bell and I. Blaekkan (2018), How do normal faults grow?, Journal of Structural Geology. https://doi.org/10.1016/j.jsg.2018.08.005

Saemundsson, K. (1992), Geology of the Thingvallavatn Area, Oikos, 64(1/2), 40-68. doi:10.2307/3545042

Sgambato, C., J. P. Faure Walker, G. P. Roberts (2020), Uncertainty in strain-rate from field measurements of the geometry, rates and kinematics of active normal faults: Implications for seismic hazard assessment, Journal of Structural Geology, Volume 131, https://doi.org/10.1016/j.jsg.2019.103934.

Sinton, J., K. Gronvold, and K. Sæmundsson (2005), Postglacial eruptive history of the Western Volcanic Zone, Iceland, Geochem. Geophys. Geosyst., 6, Q12009, doi:10.1029/2005GC001021

Sonnette, L., J. Angelier, T. Villemin, and F. Bergerat (2010), Faulting and fissuring in active oceanic rift: Surface expression, distribution and tectonic–volcanic interaction in the Thingvellir Fissure Swarm, Iceland. Journal of Structural Geology, 32(4), 407-422. https://doi.org/10.1016/j.jsg.2010.01.003

Tentler, T., and Mazzoli, S. (2005), Architecture of Normal Faults in the Rift Zone of Central North Iceland, Journal of Structural Geology, vol. 27, no. 9, pp. 1721–1739., doi:10.1016/j.jsg.2005.05.018.

Trippanera, D., V. Acocella, J. Ruch, and B. Abebe (2015), Fault and graben growth along active magmatic divergent plate boundaries in Iceland and Ethiopia, Tectonics, 34, doi:10.1002/2015TC003991.

570 Villemin, T., and Bergerat, F. (2013), From surface fault traces to a fault growth model: the
571 Vogar fissure swarm of the Reykjanes Peninsula, Southwest Iceland, Journal of
572 Structural Geology, 51, 38-51. https://doi.org/10.1016/j.jsg.2013.03.010
573 Walsh, J. J., W. R. Bailey, C. Childs, A. Nicol and C. G. Bonson (2003), Formation of
574 segmented normal faults: a 3-D perspective. Journal of Structural Geology, 25(8),
575 1251-1262. https://doi.org/10.1016/S0191-8141(02)00161-X
576 Walsh, J. J., A. Nicol and C. Childs (2002), An alternative model for the growth of faults.
577 Journal of Structural Geology, 24(11), 1669-1675. https://doi.org/10.1016/S0191-
578 8141(01)00165-1
579 Whittaker, A. C., P. A. Cowie, M. Attal, G. E. Tucker, and G. P. Roberts (2007), Bedrock
580 channel adjustment to tectonic forcing: Implications for predicting river incision rates.
581 Geology, 35(2), 103-106.
582 Wilkinson, M., G. P. Roberts, K. McCaffrey, P. A. Cowie, J. P. Faure Walker, I.
583 Papanikolau, R. J. Phillips, A. M. Michetti, E. Vittori, L. Gregory, L. Wedmore, Z. K.
584 Watson (2015), Slip distributions on active normal faults measured from LiDAR and
585 field mapping of geomorphic offsets: an example from L'Aquila, Italy, and
586 implications for modelling seismic moment release, *Geomorphology*, *237*, 130–141,
587 doi:10.1016/j.geomorph.2014.04.026.
588 Wolfe, C. J., I. T. Bjarnason, J. C. VanDecar and S. C. Solomon (1997), Seismic structure of
589 the Iceland mantle plume. Nature, 385(6613), 245. https://doi.org/10.1038/385245a0
590

591 **Figure Captions**

592

593 Figure 1 – Background literature on the relationship between the local fault geometry and the
594 along-strike distribution of throw and throw-rate. a) Natural example from the 2016 seismic

595 sequence in Central Italy, which ruptured twice the same portion of the Mt. Vettore fault, of
596 steeper fault dip and large coseismic throws within an along-strike fault bend, when
597 compared to values immediately outside the fault bend (modified after Iezzi et al., 2018). b)
598 Theoretical studies showing how a variation of fault strike and dip within along-strike fault
599 bends affect the value of throw rates within the bend (modified from Faure Walker et al.,
600 2009). c) Diagrams showing the interplay between fault activity and resurfacing lavas
601 (modified from Podolsky and Roberts, 2008).
602
603 Figure 2 – Location map of the study areas. a) Regional setting of Iceland. In red are
604 highlighted the neovolcanic zones, centre of the continental spreading (modified after Wolfe
605 et al., 1997; Bergerat and Angelier, 2000; Einarsson, 2008). Black arrows indicate the
606 direction of regional extension (after Lafemina et al., 2005). b) Map of the WVZ, with
607 highlighted the Thingvellir rift and the Hengill volcanic complex. c) Map of the Thingvellir
608 rift. In red are the faults subject of this study, in black are other principal faults of the
609 Thingvellir rift (defined with our fieldwork and modified after Gudmundsson, 1987;
610 Saemundsson, 1992; Sinton et al., 2005; Sonnette et al., 2010). Lava units are after Sinton et
611 al., 2005. d) Map of the Hengill volcanic complex. In red are the faults studied within this
612 paper, in black are other principal faults.
613
614 Figure 3 – Cartoons of the field measurements. a) Cartoon of the Almannagja fault. It shows
615 the presence of an inner graben and a prominent monocline connecting footwall and
616 hangingwall. The throw has been measured as the vertical distance between the inflection
617 point and the top of the footwall. b) Cartoon of the extension fractures located within the
618 footwall of the fault in the linkage zones between the principal fault segments of the
619 Almannagja fault. c) Cartoon of the field measurements on WDf1, WDf2, WDf3. It shows

620 that these faults are characterized by a dilatational component between hangingwall and
621 footwall. The throw has been measured as the vertical distance between the hangingwall and
622 the footwall. d) Cartoon of the field measurements on WDf4 and Hengill faults. The faults
623 present a prominent fault scarp with slope deposits on it. The throw has been measured
624 reconstructing the geometry of the erosional surfaces on the hangingwall and footwall.
625
626 Figure 4 – Field photos of the Almannagja fault. a) Northward view of the fault. It shows the
627 presence of different fault segments, linked by extension fractures in the footwall; the
628 presence of an inner graben-like structure, delimited westward by sets of antithetic faults; a
629 prominent monocline which connects the footwall to the hangingwall. b) Hangingwall view
630 of the Almannagja fault. It shows how the fault and the monocline are continuous along the
631 strike. c) Across-strike view of the Almannagja fault showing the direction across which the
632 profiles were constructed. d) View inside the inner graben. It highlights the presence of
633 extension fractures linking en-echelon principal segments and the presence of antithetic
634 faults. e) View of the southern sector of the Almannagja fault. It shows that the inflection line
635 is below the lake level, and therefore it was not possible to collect measurements in this
636 sector of the fault. f) View of the southern tip of the Almannagja fault. It shows how the fault
637 is characterized by extension fractures, across which the vertical offset is less than 1 m.
638
639 Figure 5 – Structural map of the Almannagja fault. In red is the principal trace of the
640 Almannagja fault. In blue are extension fractures, in pale blue is the inflection line of the
641 monocline. The location of the WDf1 and WDf2 (thinner red and blue lines) are shown. In
642 black are other faults of the Thingvellir rift. Geological units are from Saemundsson, 1992,
643 and Sinton et al., 2005.
644

Figure 6 – Detailed structural map of the Almannagja fault. This figure shows in detail the geometry and the structure of the Almannagja fault. Locations of a), b), c) and d) are shown in Figure 5. In red are the principal fault segments, in blue are the extension fractures, in orange are the antithetic faults, and in pale blue is the inflection line of the monocline. In white are the offset measurements with a complete profile of the monocline. In yellow are offset measurements without a profile of the monocline.

Figure 7 – Along-strike throw profile of the Almannagja fault. Measurements of the top of the footwall and of the top of the monocline have been normalized for the inflection line. Therefore, measurements of the top of the footwall represent the throw of the fault. In green is the range of the throw-rates of the fault, calculated for the time constraint of 9 and 10.2 ka (from the age of dissected lava units, Sinton et al., 2005). Our suggested principal segmentation of the Almannagja fault is shown. Note that the throw and throw-rates increase within an along-strike fault bend.

Figure 8 – Study of the drainage in the footwall of the Almannagja fault. a) Location map of the river bed in the footwall of the Almannagja fault. b) Northward migration of the river bed in relationship to the increased uplift following the fault linkage. c) Blockage of the river and production of the waterfall following fast footwall uplift and fault linkage. d) The photo shows that the waterfall does not show an incised channel in the footwall, which reflects a recent formation of the waterfall. Overall this figure shows that the fault linkage processes are influencing the drainage across the fault.

Figure 9 – Field photos of the W-Dipping faults in the Thingvellir rift. a) Along strike view of the WDf1. It highlights the presence of multiple fault segments and of the extensional

fractures linking these en echelon faults (people as scale). b) Across strike view of the WDf1. It highlights the dilatational component of the fault and the presence of water infilling the inner graben. c) Along strike view of the WD2 showing the flat hangingwall and footwall surfaces and the dilatational component of the fault. d) Across strike view of the WDf2 highlighting the vertical offset between the hangingwall and the footwall of the fault. e) Along strike view of the WDf3. It shows the undisturbed hangingwall and footwall surfaces and the dilatational component of the fault. f) View of the fault bend along WDf3. An incipient fault bend is propagating through a relay ramp connecting two principal fault segments. A road ~5 m wide is located across the relay ramp. g) Panoramic view of the WDf4 showing the continuity of the prominent fault scarp. h) View of the fault scarp across WDf4. Green arrows mark a fault scarp profile collected across the fault.

Figure 10 – Structural maps of the W-Dipping faults. a) The structural fault maps of the WDf1 and WDf2, located immediately in front of the Almannagja fault. In red are the principal fault traces, in blue are the extension fractures, in black are other fault traces. In yellow are the location of the measurements of the throw. b) The structural fault maps of the WDf3 and WDf4, located on the eastern flank of the Thingvellir rift. In red are the principal fault segments mapped, in blue are the extension fractures, in orange are antithetic faults, in black are other principal faults, not mapped in detail in this study. For WDf3, the dashed lines mark the sector of the fault along which field measurements have been collected from the measurement location (see text for details). For WDf4, fault scarp profiles used to measure the throw are shown in white. Geological units are from Sinton et al., 2005.

Figure 11 – Along-strike throw profiles of the W-Dipping faults. In black are the measurements of throw. In green are the range of the throw rate values, constrained using the

695 age of the lava flows which the faults are propagating through (see Figure 9). For the WDf1
696 and WDf2, the throw rate profiles coincide with the throw profile because of the single value
697 for the age of the lava flows.
698
699 Figure 12 – Field photos of the Hengill volcanic complex. a) Panoramic view of the study
700 area. The three principal fault segments identified in the area are marked with the different
701 coloured arrows. The white arrows mark the subglacial erosional surfaces used to constrain
702 the throw across the faults. b) Linkage zone between Fault 1 and Fault 3, with a relay ramp
703 located between the two. It is also evidenced the presence of a landslide affecting the fault
704 scarp. Measurements have not been collected in the presence of landslides. c) Erratic
705 boulders on the subglacial erosional surfaces, confirming the glacial origin of the surfaces. d)
706 Outcrop of a fault plane along Fault 3. Field measurements show dip slip kinematics for the
707 fault. e) Panoramic view from the hangingwall of the studied faults. The coloured arrows
708 show the principal faults, with the subglacial erosional surfaces shown in white. The along-
709 strike fault bend in Fault 1 is shown.
710
711 Figure 13 – Structural fault map of the faults studied in the Hengill volcanic complex. In red
712 are the principal faults studied, in black are other principal faults. In yellow are marked the
713 subglacial erosional surfaces, in orange are reported the slope deposits on the fault scarps, in
714 blue is marked a lake bed in the hangingwall of the fault. In white are reported the traces of
715 the fault scarp profiles. White stars mark the locations of outcrops of the fault plane.
716
717 Figure 14 – Along-strike throw profiles for the faults in the Hengill volcanic complex. It
718 shows the presence of along-strike fault bends along Fault 1 and Fault 3, across which the
719 throw increases. The shaded blue area in the profile is the range of throw-rates for the faults,

720 constrained with the age of deglaciation and exposure of the subglacial erosional surfaces
721 (from Licciardi et al., 2007). It is also reported the presence of a lake bed in the hangingwall
722 of the fault, located in front of the fault bend and in correspondence of the maximum throw
723 measured. This shows that the fault bend has influenced the drainage system in the
724 hangingwall of the fault.
725
726 Figure 15 – Fault growth model showing that fault bends present faster throw rates, compared
727 to the throw-rates on faults immediately outside the bend, since the onset of the fault linkage
728 processes.

(a) Natural dataset of large coseismic throw and steeper fault dip within along-strike fault bends, Mt. Vettore 2016 earthquakes (Central Italy) (modified after Iezzi et al., 2018)

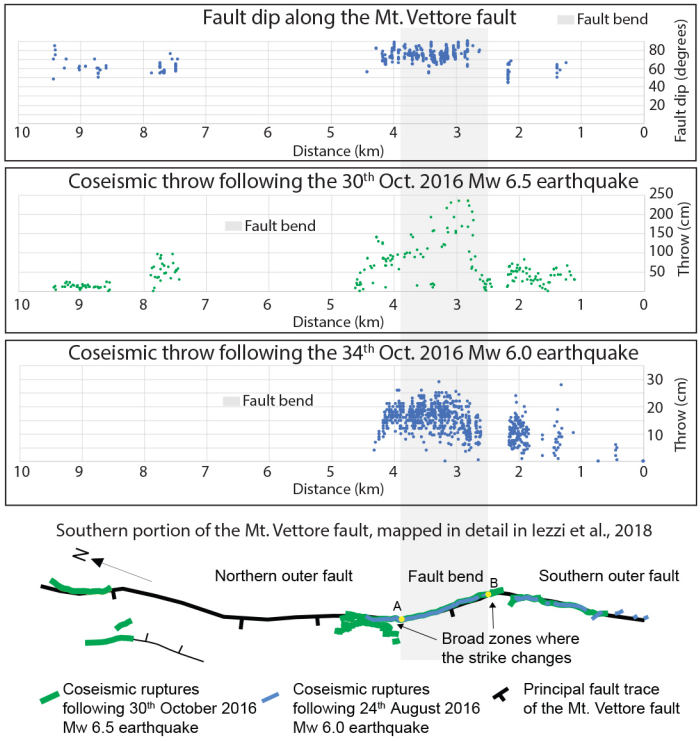

(b) Theoretical studies showing effect of fault strike and dip across the fault bend on throw-rate, assuming constant principal strain-rate (modified after Faure Walker et al., 2009)

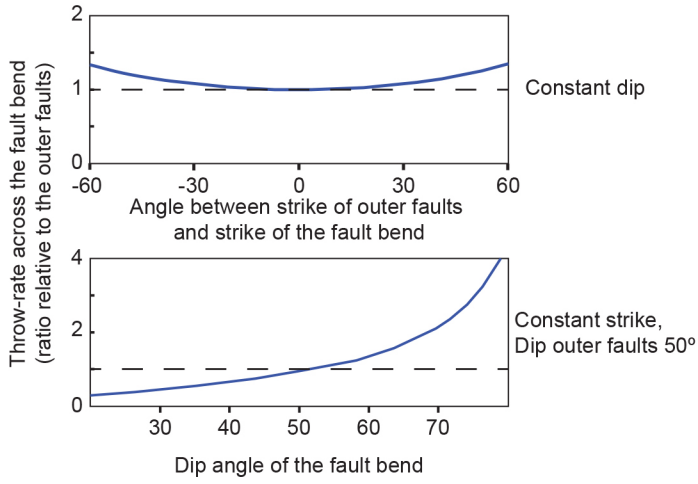

(c) Interplay between resurfacing lava flows and active faults

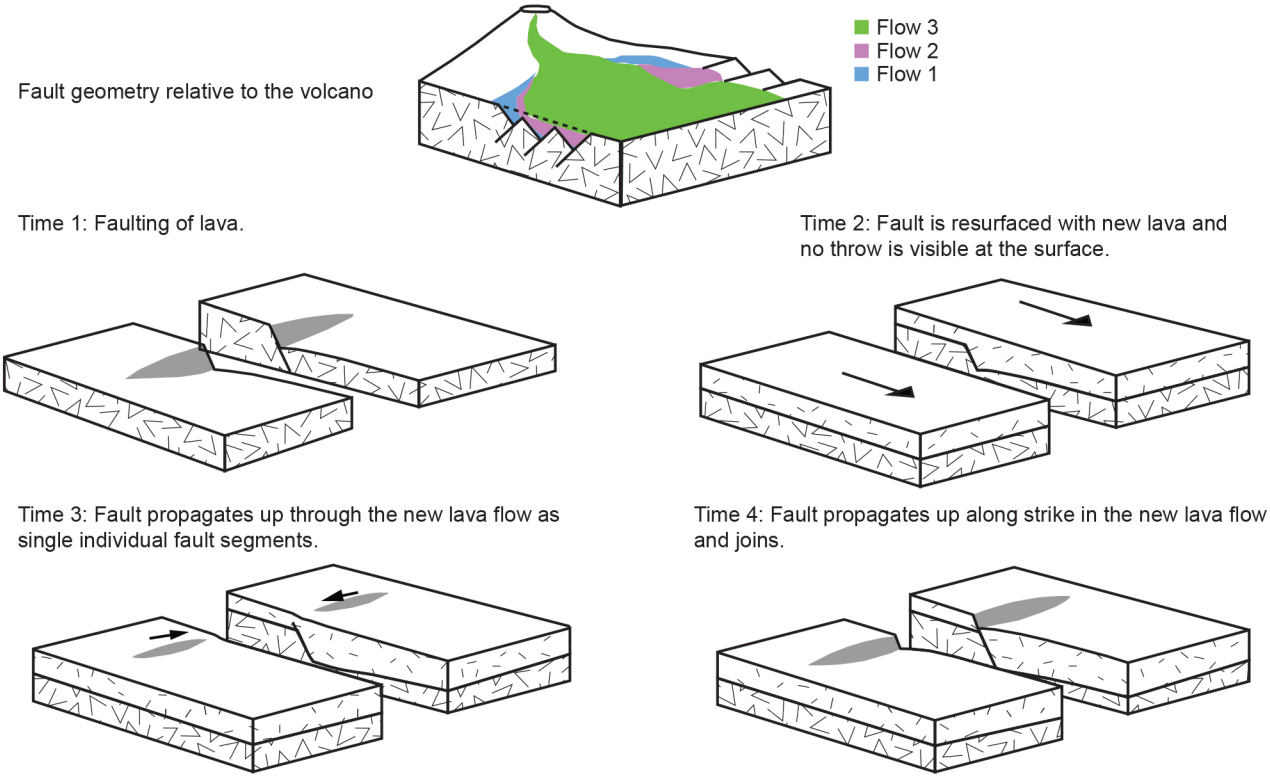

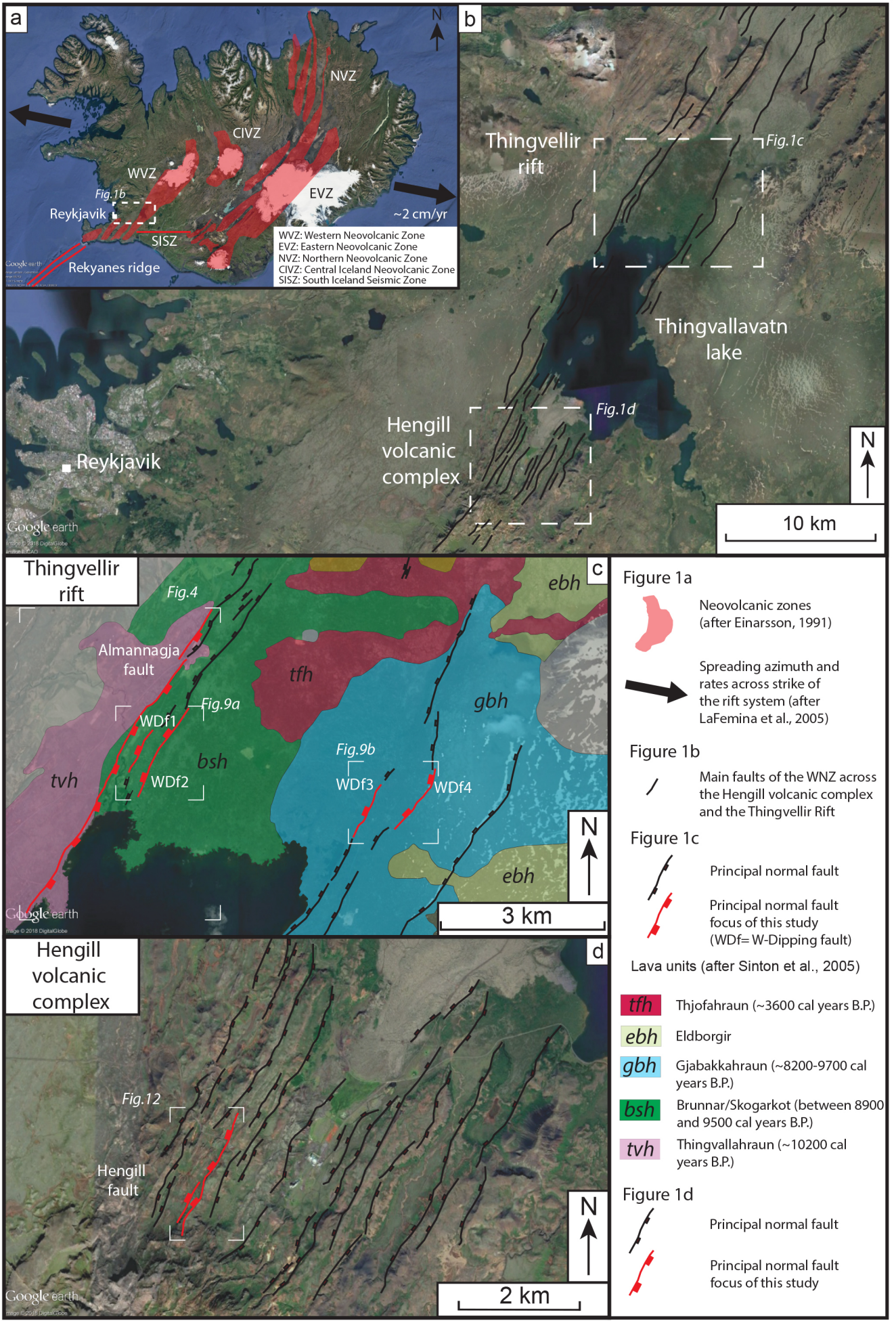
a
N
NVZ
CIVZ
WVZ
EVZ
Fig.1b
Reykjavik
SISZ
Rekyanes ridge
~2 cm/yr
WVZ: Western Neovolcanic Zone
EVZ: Eastern Neovolcanic Zone
NVZ: Northern Neovolcanic Zone
CIVZ: Central Iceland Neovolcanic Zone
SISZ: South Iceland Seismic Zone
b
Thingvellir rift
Fig.1c
Thingvallavatn lake
Hengill volcanic complex
Fig.1d
Reykjavik
N
10 km
Thingvellir rift
c
Fig.4
Almannagja fault
Fig.9a
WDf1
WDf2
tvh
bsh
tfh
ebh
gbh
Fig.9b
WDf3
WDf4
N
3 km
Hengill volcanic complex
d
Fig.12
Hengill fault
N
2 km
Figure 1a
Neovolcanic zones (after Einarsson, 1991)
Spreading azimuth and rates across strike of the rift system (after LaFemina et al., 2005)
Figure 1b
Main faults of the WNZ across the Hengill volcanic complex and the Thingvellir Rift
Figure 1c
Principal normal fault
Principal normal fault focus of this study (WDf= W-Dipping fault)
Lava units (after Sinton et al., 2005)
tfh
Thjofahraun (~3600 cal years B.P.)
ebh
Eldborgir
gbh
Gjabakkahraun (~8200-9700 cal years B.P.)
bsh
Brunnar/Skogarkot (between 8900 and 9500 cal years B.P.)
tvh
Thingvallahraun (~10200 cal years B.P.)
Figure 1d
Principal normal fault
Principal normal fault focus of this study

Almannagja fault

a) Section of the Almannagja fault with multiple antithetic faults

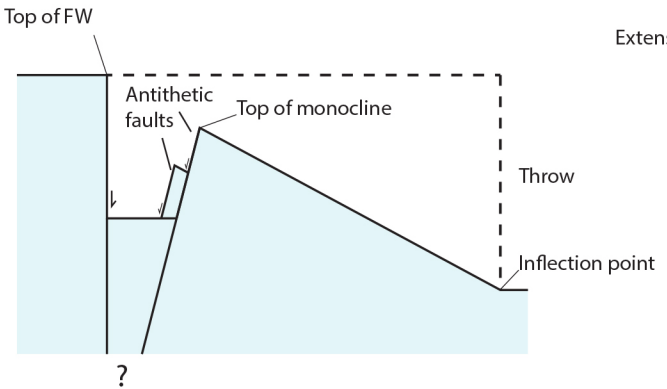

b) Extension fractures at tips of the principal fault segments of the Almannagja fault

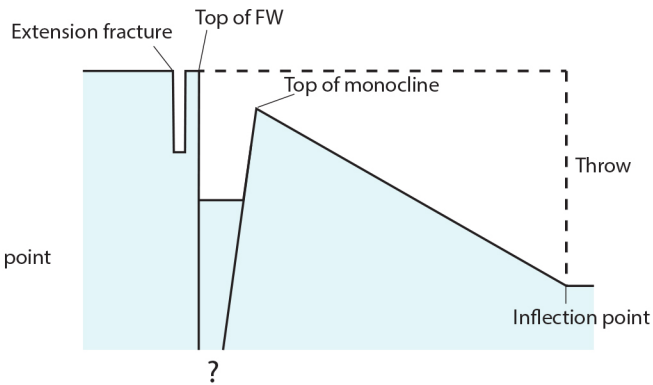

W-dipping and Hengill faults

c) W-Dipping faults 1, 2, 3

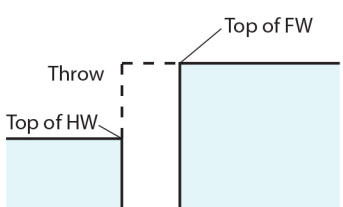

d) W-Dipping fault 4 and Hengill faults

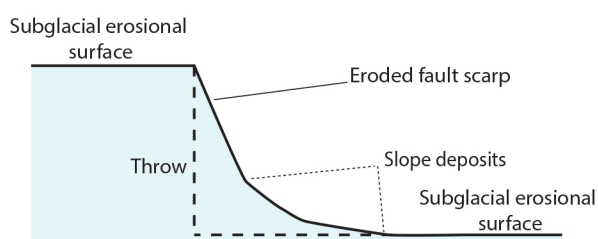


a) Northward view of the Almannagja fault
N
Extension fractures linking en-echelon fault segments
Fault segments
Across strike distributed antithetic faults delimiting the eastern flank of the graben
Monocline
West-Dipping fault 1
West-Dipping fault 2
Top footwall
Top monocline
Inflection line
b) Hangingwall view of the Almannagja fault
N
Monocline
Flat hangingwall surface
Top footwall
Top monocline
Inflection line
c) Across strike view of the Almannagja fault, along which profiles were constructed
N
Monocline
Top footwall
Top monocline
Inflection line
View inside the inner graben
d)
N
Extension fractures linking en-echelon fault segments
Fault segment
Fault segment
Antithetic faults delimiting the eastern flank of the graben
Top footwall
Top monocline
e) Southern sector of the Almannagja fault, with inflection line below the lake level
N
Inflection line not visible because it is below the lake level
Thingvallatavn lake
Top footwall
Top monocline
f) Extension fractures at the southern tip of the Almannagja fault
N
Extension fractures
Top footwall
Top monocline

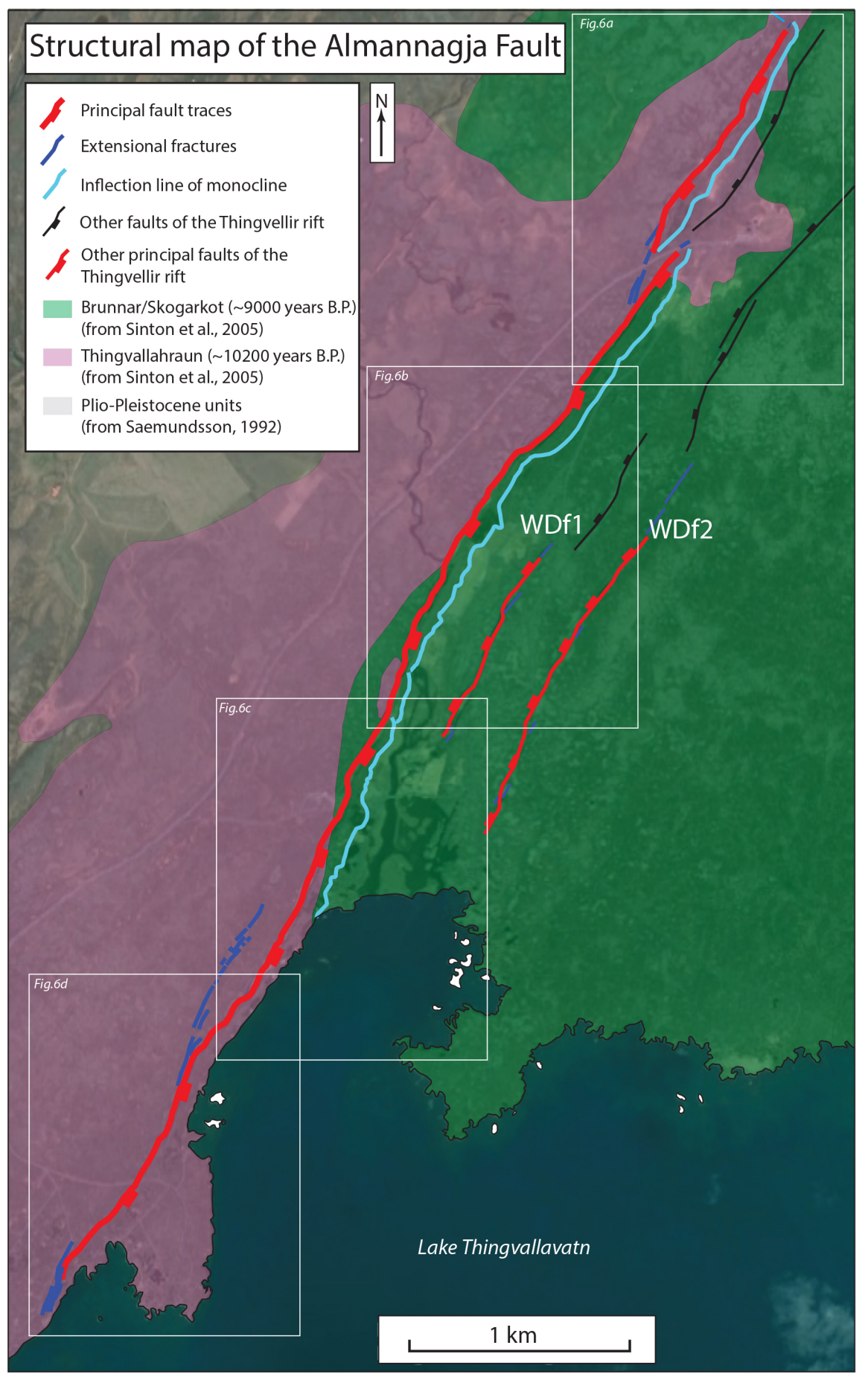
Structural map of the Almannagja Fault
Principal fault traces
Extensional fractures
Inflection line of monocline
Other faults of the Thingvellir rift
Other principal faults of the Thingvellir rift
Brunnar/Skogarkot (~9000 years B.P.) (from Sinton et al., 2005)
Thingvallahraun (~10200 years B.P.) (from Sinton et al., 2005)
Plio-Pleistocene units (from Saemundsson, 1992)
N
Fig.6a
Fig.6b
Fig.6c
Fig.6d
WDf1
WDf2
Lake Thingvallavatn
1 km

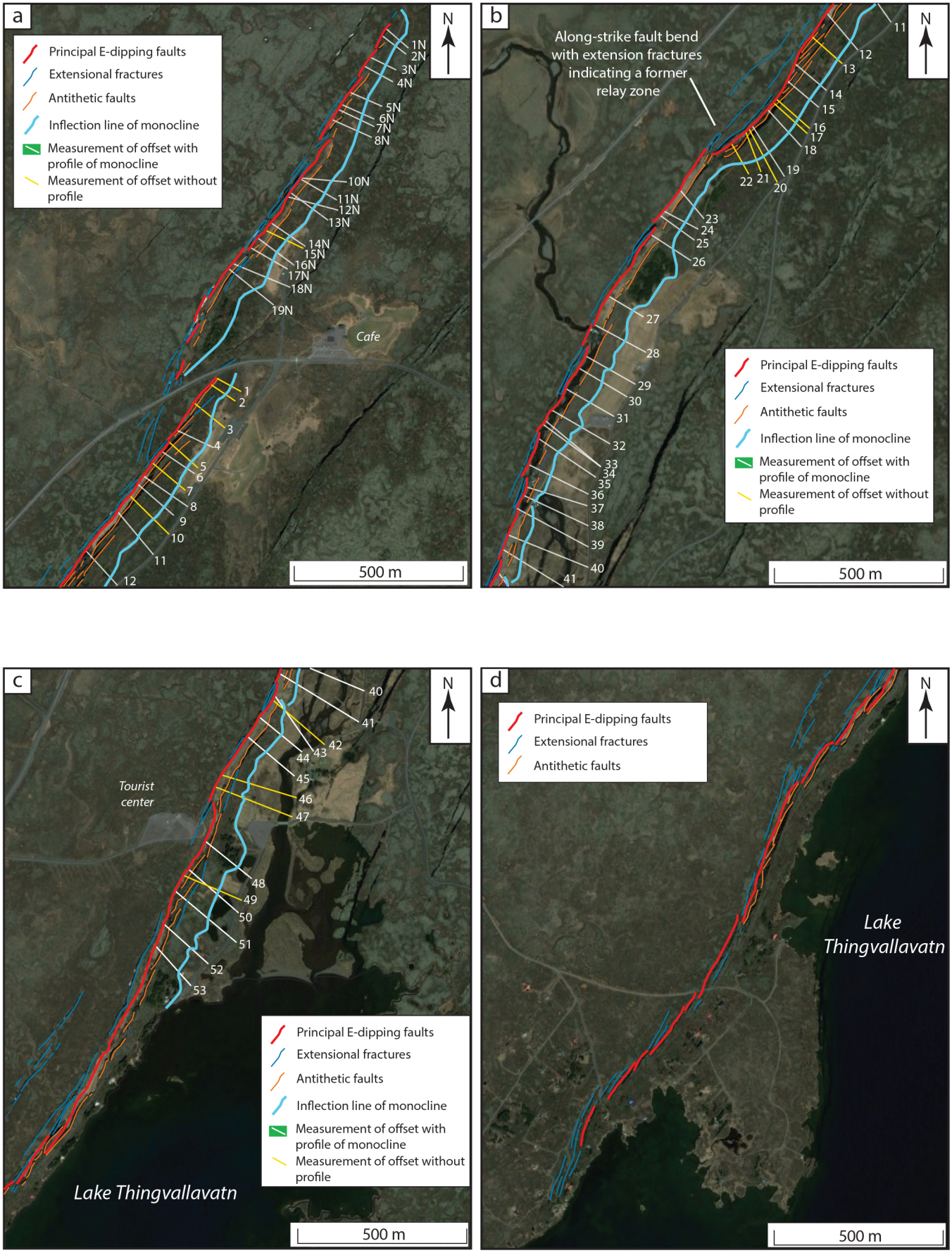
a
Principal E-dipping faults
Extensional fractures
Antithetic faults
Inflection line of monocline
Measurement of offset with profile of monocline
Measurement of offset without profile
N
1N
2N
3N
4N
5N
6N
7N
8N
10N
11N
12N
13N
14N
15N
16N
17N
18N
19N
Cafe
1
2
3
4
5
6
7
8
9
10
11
12
500 m
b
Along-strike fault bend with extension fractures indicating a former relay zone
N
11
12
13
14
15
16
17
18
19
22
21
20
23
24
25
26
27
28
29
30
31
32
33
34
35
36
37
38
39
40
41
Principal E-dipping faults
Extensional fractures
Antithetic faults
Inflection line of monocline
Measurement of offset with profile of monocline
Measurement of offset without profile
500 m
c
N
40
41
42
43
44
45
46
47
Tourist center
48
49
50
51
52
53
Principal E-dipping faults
Extensional fractures
Antithetic faults
Inflection line of monocline
Measurement of offset with profile of monocline
Measurement of offset without profile
Lake Thingvallavatn
500 m
d
Principal E-dipping faults
Extensional fractures
Antithetic faults
N
Lake Thingvallavatn
500 m

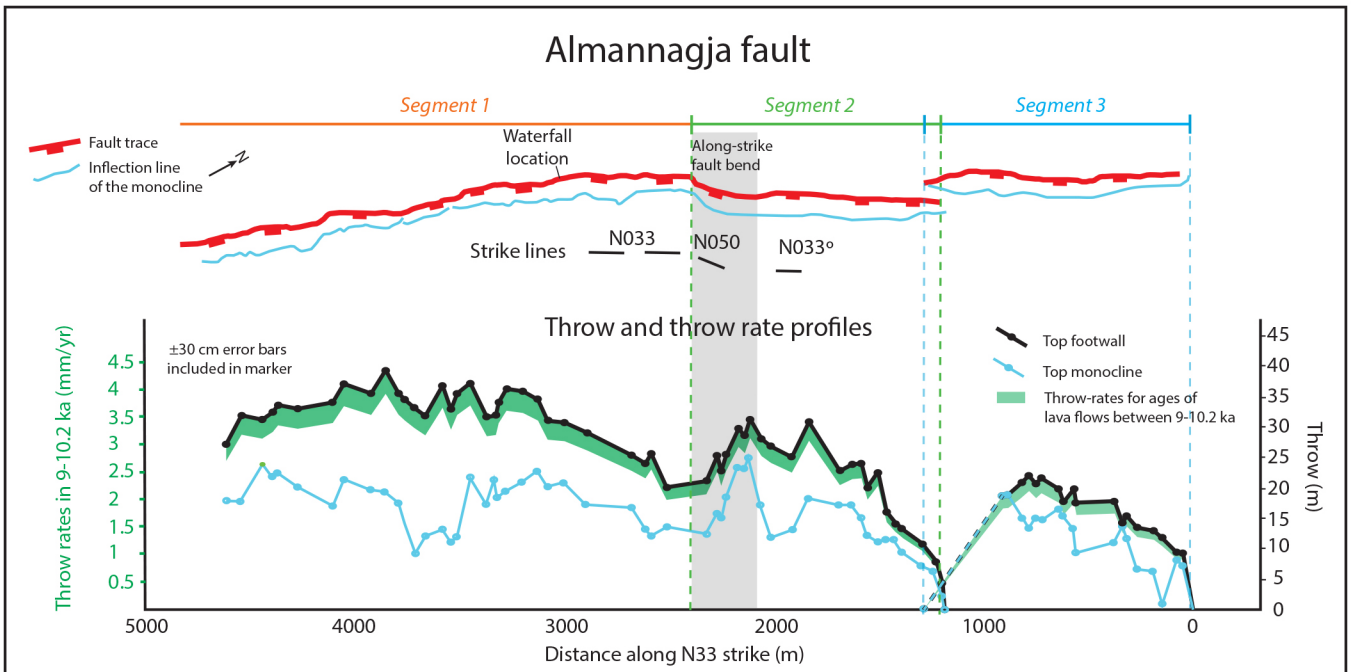
Almannagja fault
Segment 1
Segment 2
Segment 3
Fault trace
Inflection line of the monocline
N
Waterfall location
Along-strike fault bend
Strike lines
N033
N050
N033°
Throw and throw rate profiles
±30 cm error bars included in marker
Top footwall
Top monocline
Throw-rates for ages of lava flows between 9-10.2 ka
Throw rates in 9-10.2 ka (mm/yr)
Throw (m)
Distance along N33 strike (m)
4.5
4
3.5
3
2.5
2
1.5
1
0.5
45
40
35
30
25
20
15
10
5
0
5000
4000
3000
2000
1000
0

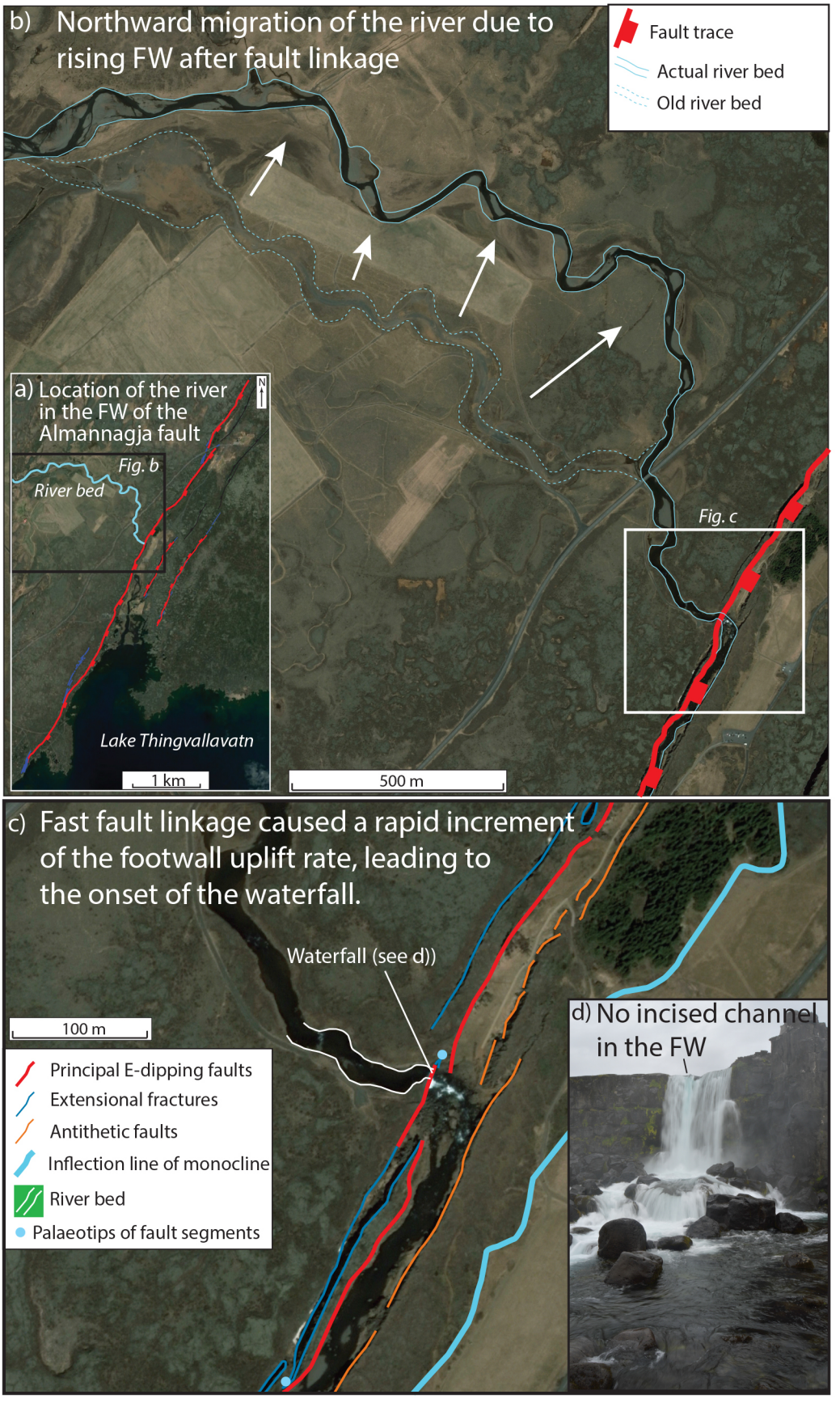
b) Northward migration of the river due to rising FW after fault linkage
Fault trace
Actual river bed
Old river bed
a) Location of the river in the FW of the Almannagja fault
N
Fig. b
River bed
Lake Thingvallavatn
1 km
Fig. c
500 m
c) Fast fault linkage caused a rapid increment of the footwall uplift rate, leading to the onset of the waterfall.
Waterfall (see d))
100 m
Principal E-dipping faults
Extensional fractures
Antithetic faults
Inflection line of monocline
River bed
Palaeotips of fault segments
d) No incised channel in the FW

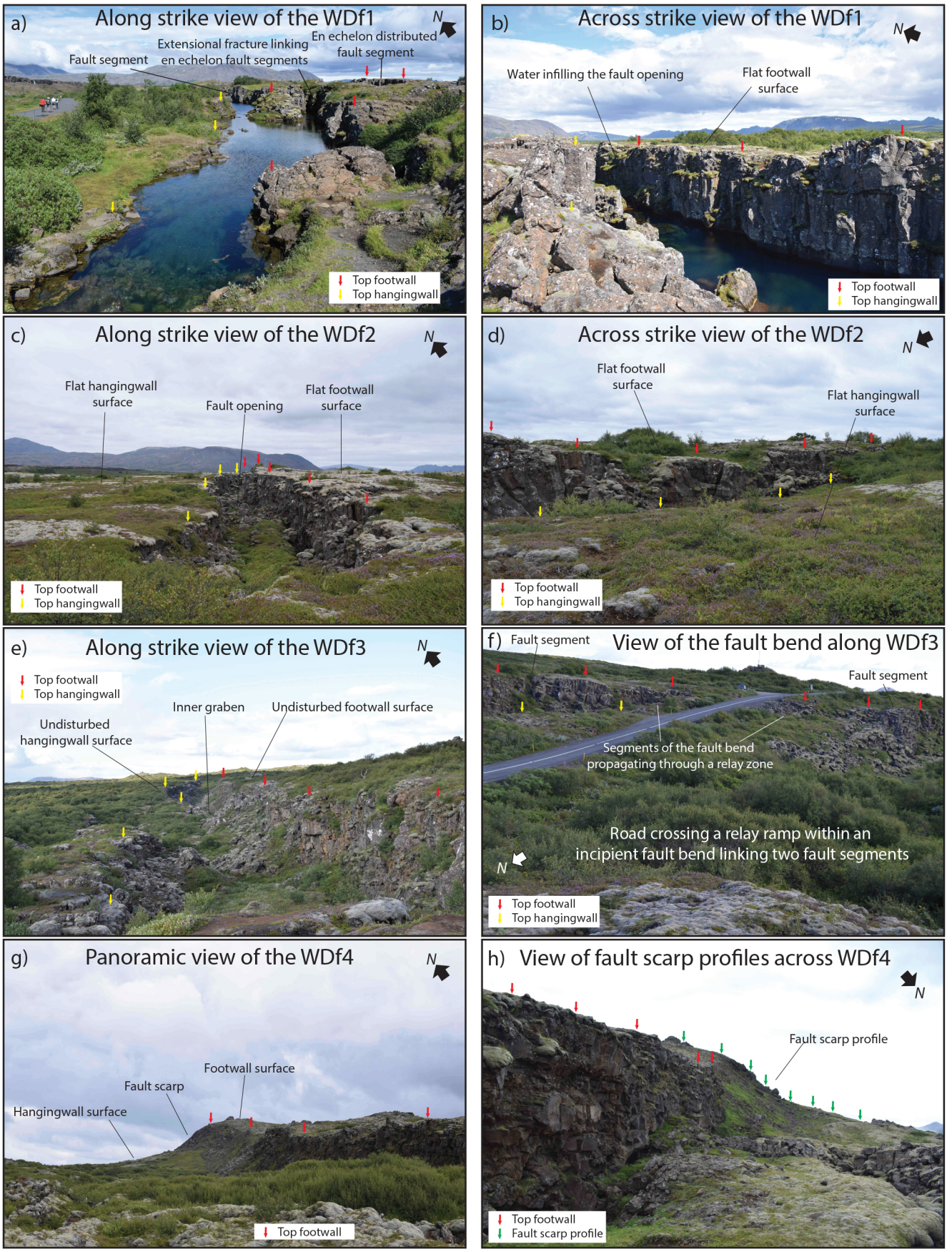
a)
Along strike view of the WDf1
N
Fault segment
Extensional fracture linking en echelon fault segments
En echelon distributed fault segment
Top footwall
Top hangingwall
b)
Across strike view of the WDf1
N
Water infilling the fault opening
Flat footwall surface
Top footwall
Top hangingwall
c)
Along strike view of the WDf2
N
Flat hangingwall surface
Fault opening
Flat footwall surface
Top footwall
Top hangingwall
d)
Across strike view of the WDf2
N
Flat footwall surface
Flat hangingwall surface
Top footwall
Top hangingwall
e)
Along strike view of the WDf3
N
Top footwall
Top hangingwall
Inner graben
Undisturbed footwall surface
Undisturbed hangingwall surface
f)
Fault segment
View of the fault bend along WDf3
Fault segment
Segments of the fault bend propagating through a relay zone
Road crossing a relay ramp within an incipient fault bend linking two fault segments
N
Top footwall
Top hangingwall
g)
Panoramic view of the WDf4
N
Footwall surface
Fault scarp
Hangingwall surface
Top footwall
h)
View of fault scarp profiles across WDf4
N
Fault scarp profile
Top footwall
Fault scarp profile

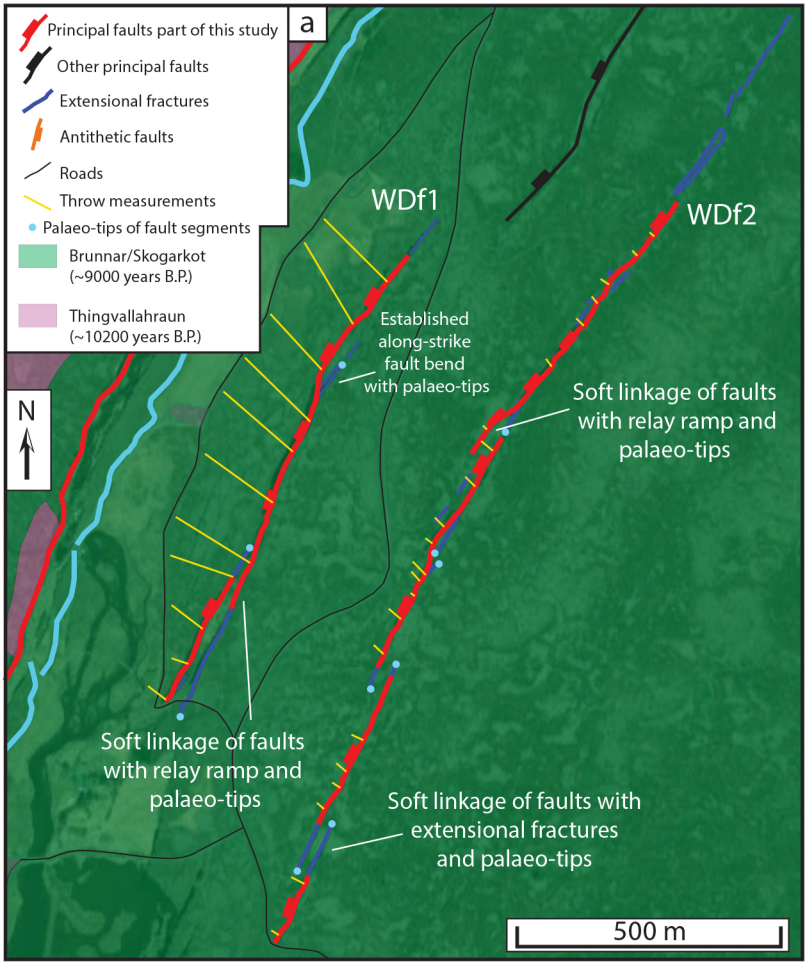
a
Principal faults part of this study
Other principal faults
Extensional fractures
Antithetic faults
Roads
Throw measurements
Palaeo-tips of fault segments
Brunnar/Skogarkot (~9000 years B.P.)
Thingvallahraun (~10200 years B.P.)
N
WDf1
WDf2
Established along-strike fault bend with palaeo-tips
Soft linkage of faults with relay ramp and palaeo-tips
Soft linkage of faults with relay ramp and palaeo-tips
Soft linkage of faults with extensional fractures and palaeo-tips
500 m

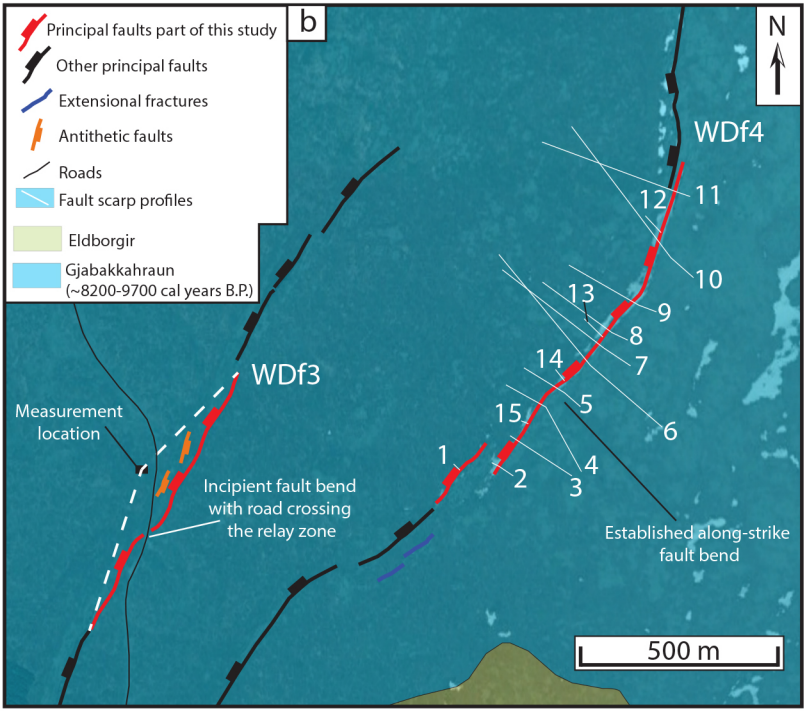
b
Principal faults part of this study
Other principal faults
Extensional fractures
Antithetic faults
Roads
Fault scarp profiles
Eldborgir
Gjabakkahraun (~8200-9700 cal years B.P.)
N
WDf4
WDf3
Measurement location
Incipient fault bend with road crossing the relay zone
Established along-strike fault bend
1
2
3
4
5
6
7
8
9
10
11
12
13
14
15
500 m

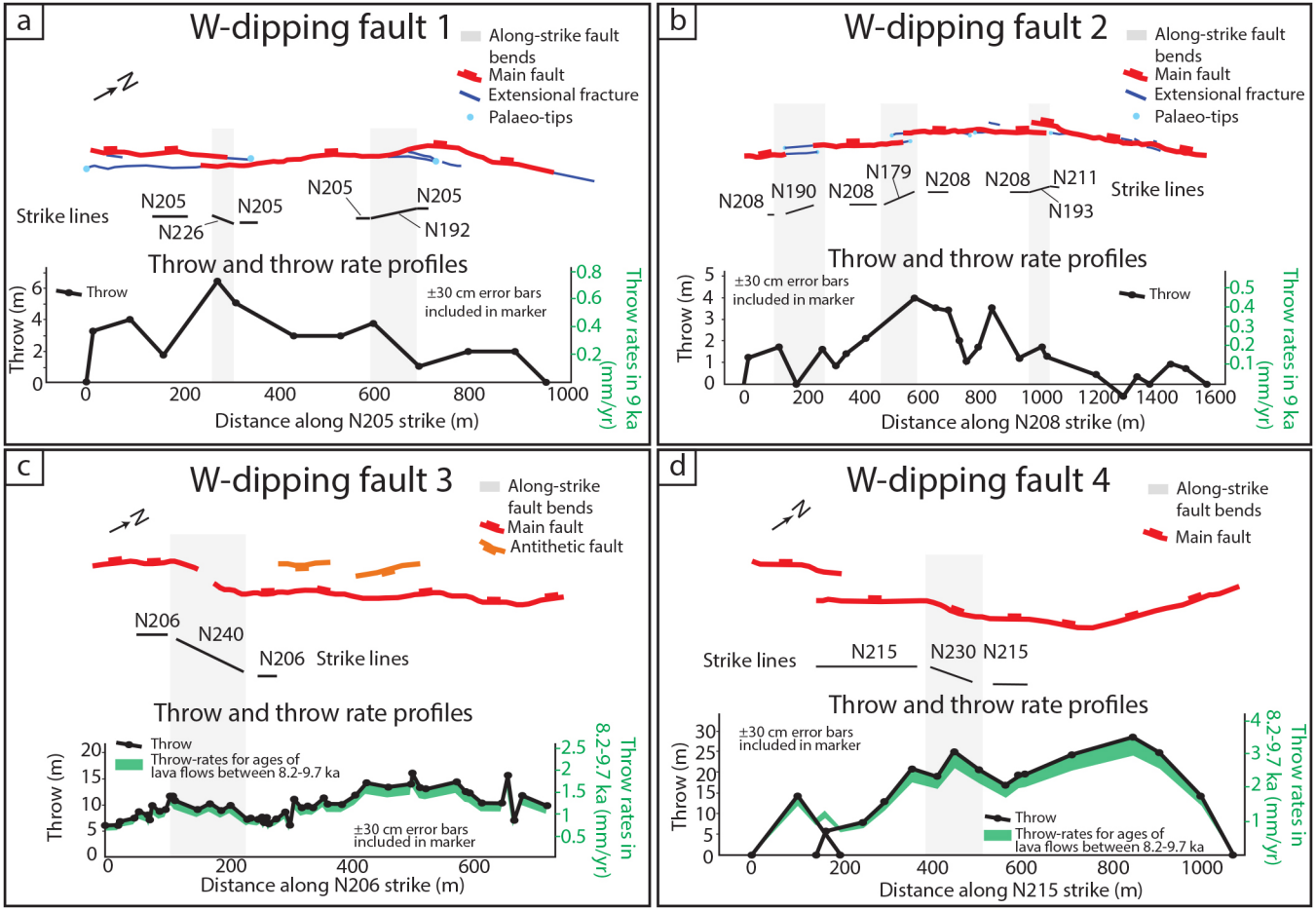
a
W-dipping fault 1
Along-strike fault bends
Main fault
Extensional fracture
Palaeo-tips
N
Strike lines
N205
N226
N205
N205
N205
N192
Throw and throw rate profiles
Throw
±30 cm error bars included in marker
Throw (m)
Throw rates in 9 ka (mm/yr)
Distance along N205 strike (m)
b
W-dipping fault 2
Along-strike fault bends
Main fault
Extensional fracture
Palaeo-tips
N208
N190
N208
N179
N208
N208
N211
N193
Strike lines
Throw and throw rate profiles
±30 cm error bars included in marker
Throw
Throw (m)
Throw rates in 9 ka (mm/yr)
Distance along N208 strike (m)
c
W-dipping fault 3
Along-strike fault bends
Main fault
Antithetic fault
N
N206
N240
N206
Strike lines
Throw and throw rate profiles
Throw
Throw-rates for ages of lava flows between 8.2-9.7 ka
±30 cm error bars included in marker
Throw (m)
Throw rates in 8.2-9.7 ka (mm/yr)
Distance along N206 strike (m)
d
W-dipping fault 4
Along-strike fault bends
Main fault
N
Strike lines
N215
N230
N215
Throw and throw rate profiles
±30 cm error bars included in marker
Throw
Throw-rates for ages of lava flows between 8.2-9.7 ka
Throw (m)
Throw rates in 8.2-9.7 ka (mm/yr)
Distance along N215 strike (m)

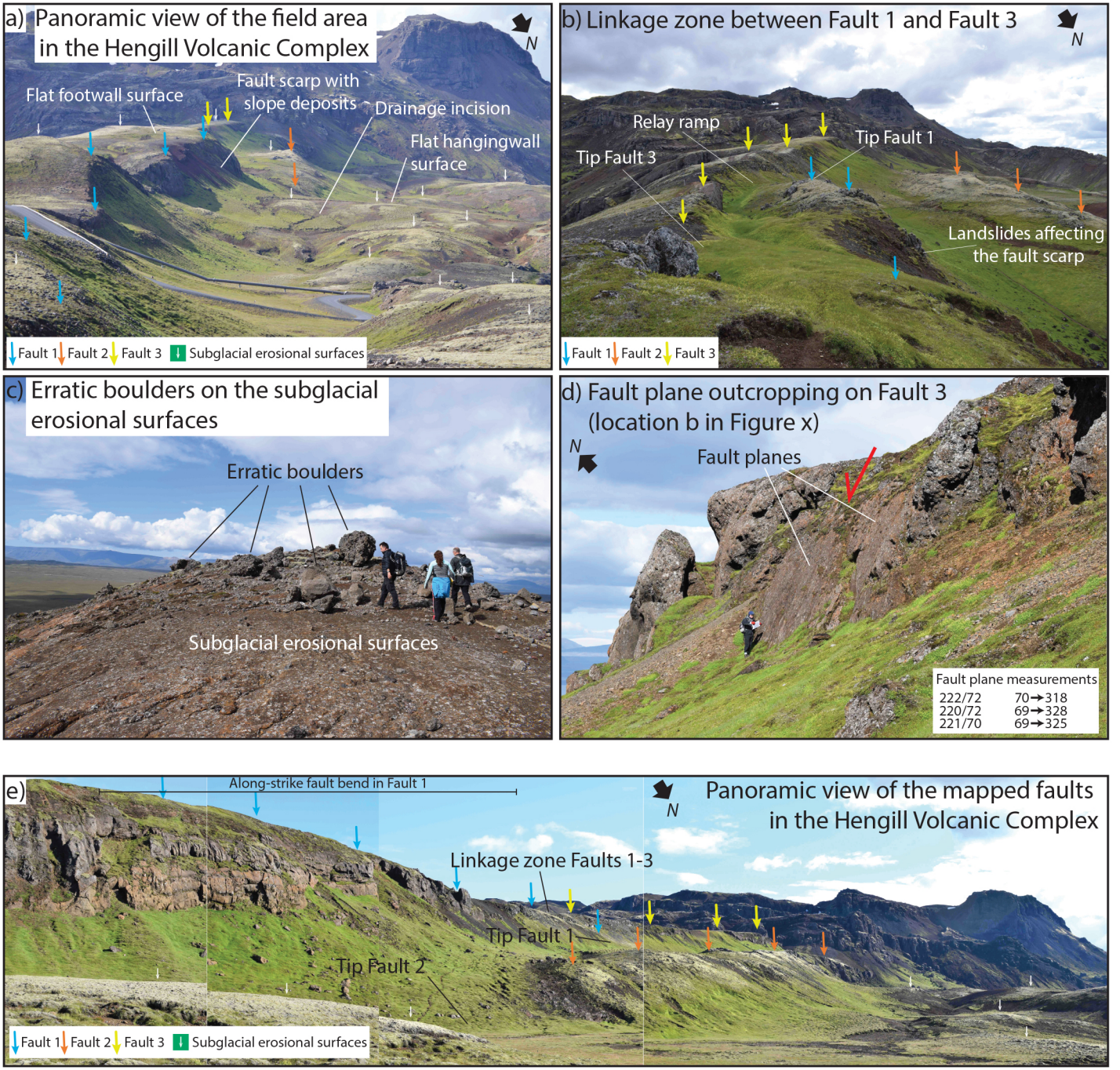
a) Panoramic view of the field area in the Hengill Volcanic Complex
N
Flat footwall surface
Fault scarp with slope deposits
Drainage incision
Flat hangingwall surface
Fault 1
Fault 2
Fault 3
Subglacial erosional surfaces
b) Linkage zone between Fault 1 and Fault 3
N
Relay ramp
Tip Fault 1
Tip Fault 3
Landslides affecting the fault scarp
Fault 1
Fault 2
Fault 3
c) Erratic boulders on the subglacial erosional surfaces
Erratic boulders
Subglacial erosional surfaces
d) Fault plane outcropping on Fault 3 (location b in Figure x)
N
Fault planes
Fault plane measurements
222/72 70→318
220/72 69→328
221/70 69→325
e)
Along-strike fault bend in Fault 1
N
Panoramic view of the mapped faults in the Hengill Volcanic Complex
Linkage zone Faults 1-3
Tip Fault 1
Tip Fault 2
Fault 1
Fault 2
Fault 3
Subglacial erosional surfaces

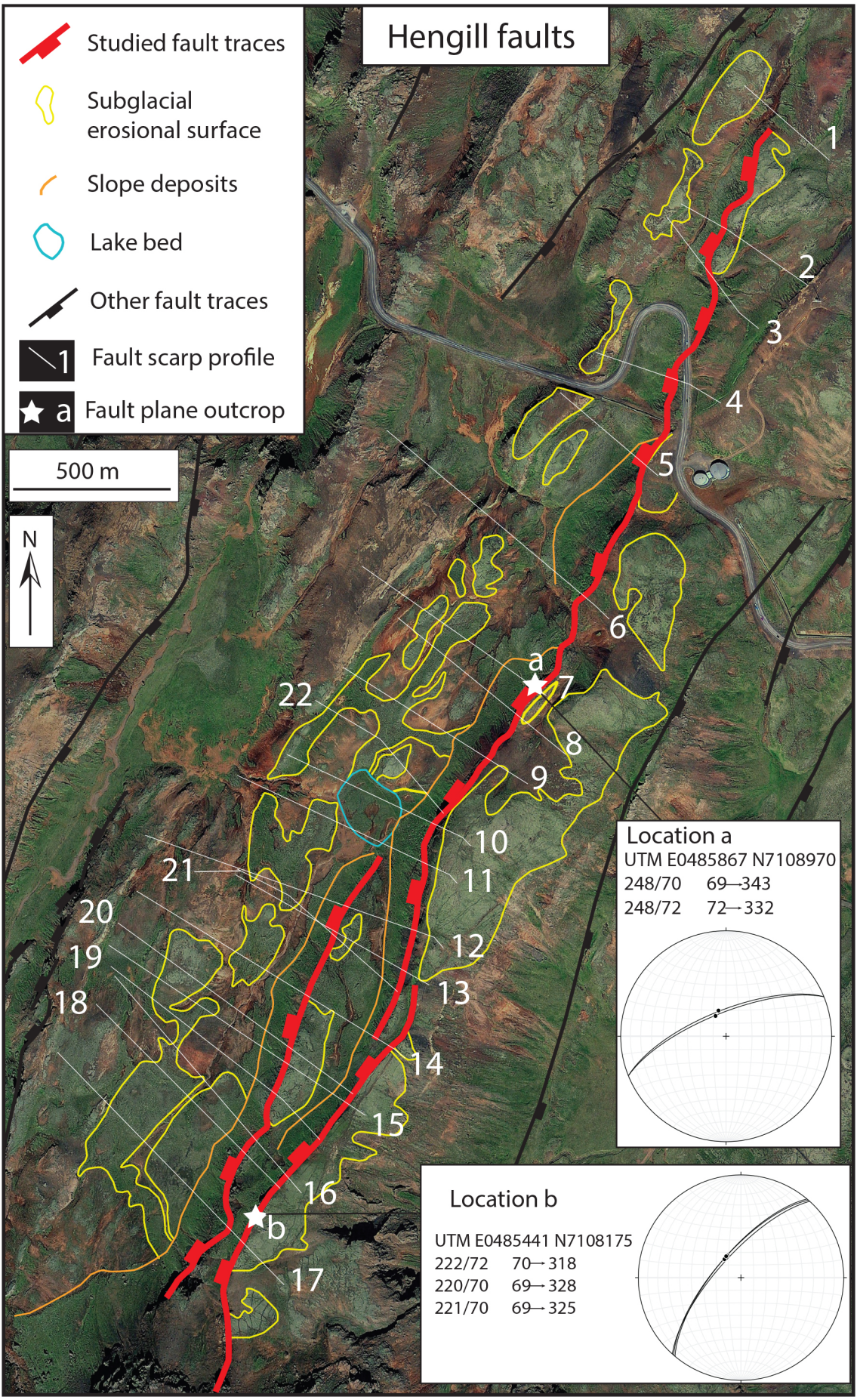
Hengill faults
Studied fault traces
Subglacial erosional surface
Slope deposits
Lake bed
Other fault traces
1 Fault scarp profile
a Fault plane outcrop
500 m
N
1
2
3
4
5
6
a
7
8
9
10
11
12
13
14
15
16
b
17
18
19
20
21
22
Location a
UTM E0485867 N7108970
248/70 69→343
248/72 72→332
Location b
UTM E0485441 N7108175
222/72 70→318
220/70 69→328
221/70 69→325

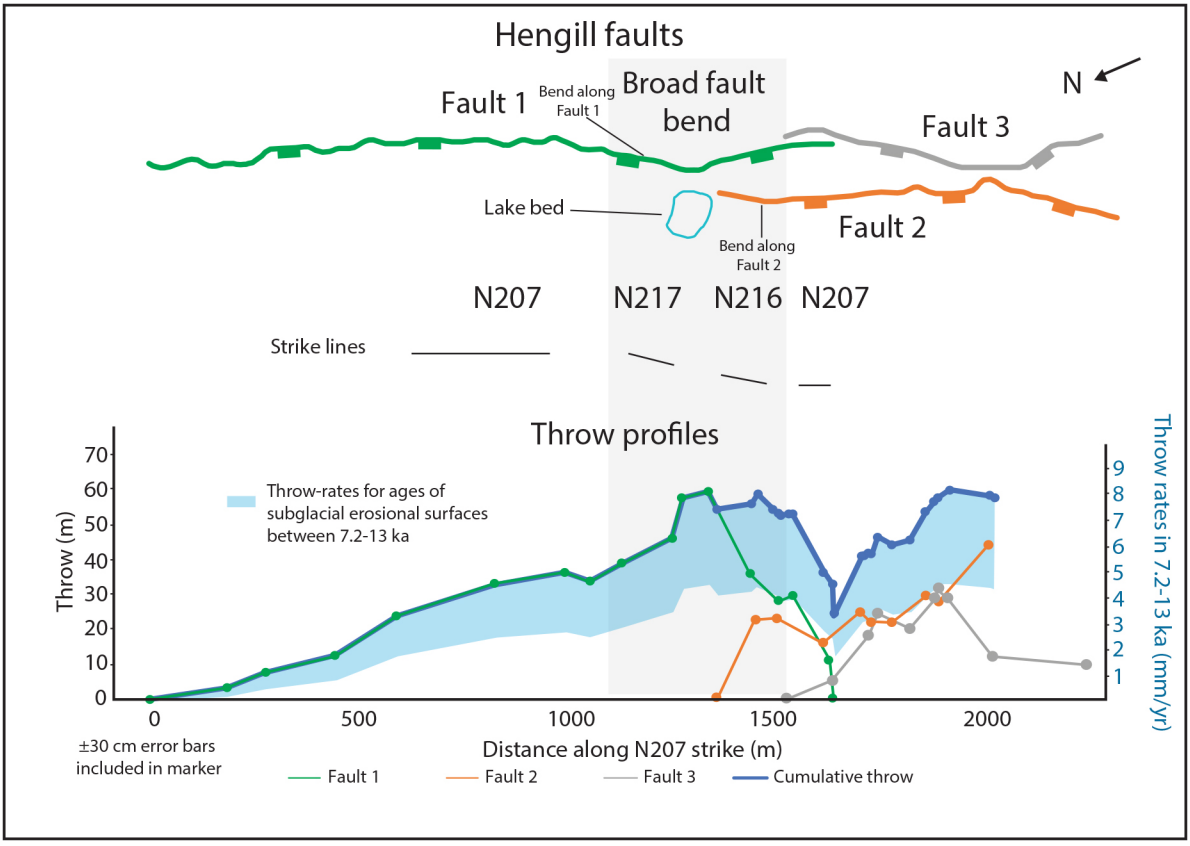
Hengill faults
Fault 1
Bend along Fault 1
Broad fault bend
Fault 3
N
Lake bed
Fault 2
Bend along Fault 2
N207
N217
N216
N207
Strike lines
Throw profiles
Throw-rates for ages of subglacial erosional surfaces between 7.2-13 ka
Throw (m)
Throw rates in 7.2-13 ka (mm/yr)
±30 cm error bars included in marker
Distance along N207 strike (m)
Fault 1
Fault 2
Fault 3
Cumulative throw

(a)

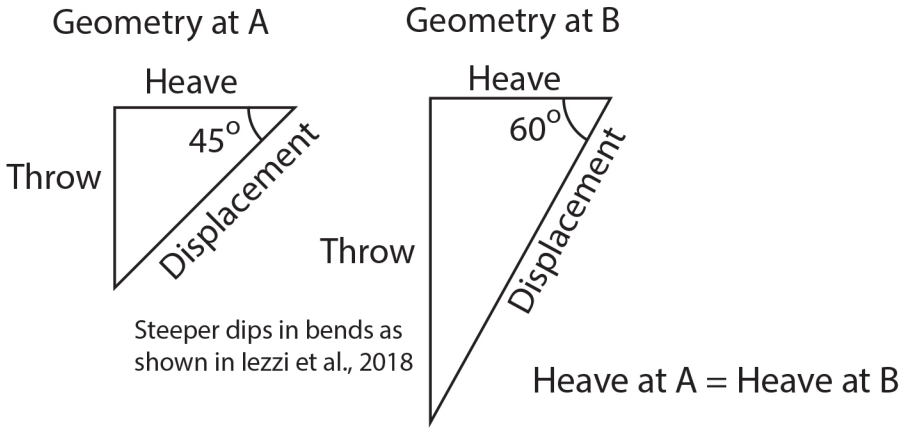

(b)

Time 0

Single fault segments, no linkage

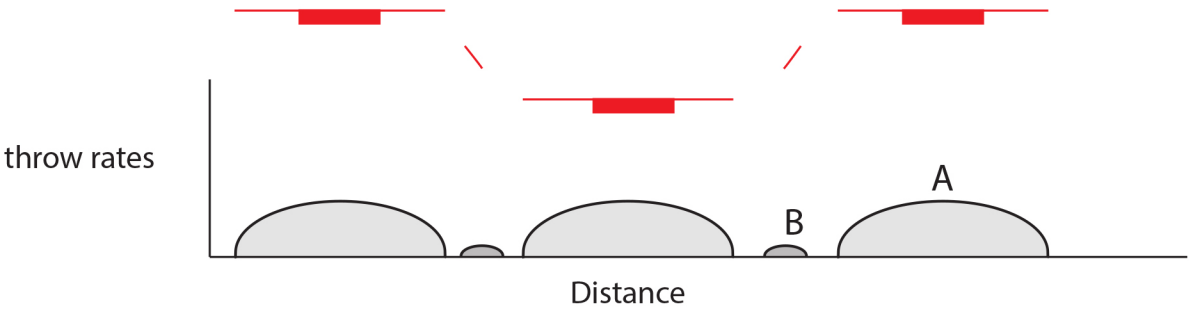

Time 1

Fault linkage starts, incipient fault bends develop,
throw rates in linkage zones are faster than rates on fault segments

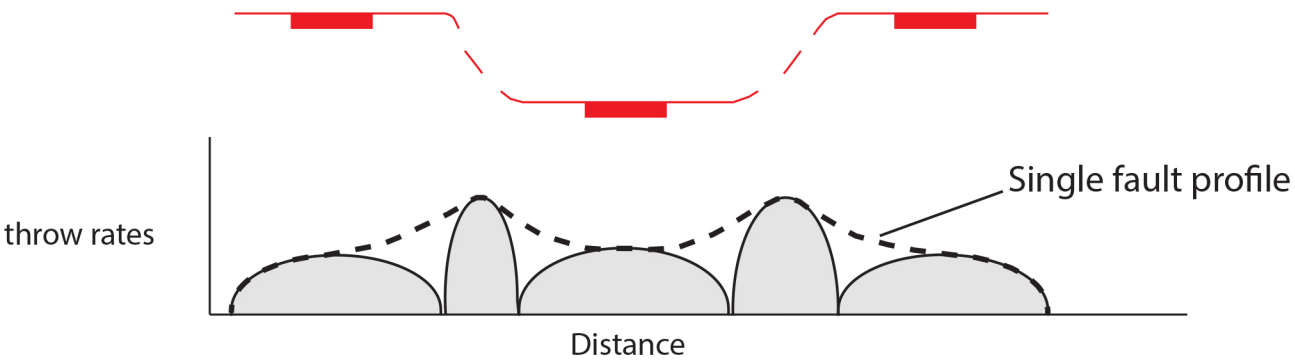

Time 2

Fault linkage is complete, fault bends established, throw rates increase along the fault, with maxima within the bends.